

**Quantification of the Energetic and Microcirculatory
Heterogeneity in the Renal System**

by

Matthew J. McCarroll

B.S. in Chemical and Petroleum Engineering, University of
Pittsburgh, 2016

Submitted to the Graduate Faculty of
the the Swanson School of Engineering in partial fulfillment
of the requirements for the degree of

Master of Science

University of Pittsburgh

2019

UNIVERSITY OF PITTSBURGH
SWANSON SCHOOL OF ENGINEERING

This thesis was presented

by

Matthew J. McCarroll

It was defended on

July 25, 2019

and approved by

Robert S. Parker, Ph.D., Professor, Department of Chemical and Petroleum Engineering

Gilles Clermont, M.D., Department of Critical Care Medicine

Jason Shoemaker, Ph.D., Professor, Department of Chemical and Petroleum Engineering

Thesis Advisors: Robert S. Parker, Ph.D., Professor, Department of Chemical and

Petroleum Engineering

Gilles Clermont, M.D., Department of Critical Care Medicine

Copyright © by Matthew J. McCarroll
2019

Quantification of the Energetic and Microcirculatory Heterogeneity in the Renal System

Matthew J. McCarroll, M.S.

University of Pittsburgh, 2019

Acute kidney injury (AKI) is a syndrome characterized by the rapid loss of kidney function and is typically diagnosed by an increase in blood-urea-nitrogen and serum creatinine, a decrease in the glomerular filtration rate (GFR), and a decrease in urine output. AKI can be brought on by a myriad of events: physical damage to the kidney, cardiac arrest, blood loss, toxicologic effects from pharmacological drug use, and in most cases seen, sepsis. These events introduce global and or local ischemic insult to the kidney, causing a decrease in renal functionality. Originally, global renal hypoperfusion was thought to be the culprit causing AKI. However, evidence is showing that AKI can occur in the absence of this, proved by the normal or even increased blood flow seen in sepsis-induced AKI. In fact, studies are finding similar results that show microcirculatory dysfunction, inflammation, and tubular oxidative stress are the driving physiological factors for sepsis-induced AKI.

The development and use of intravital video microscopy (IVVM) allows *in vivo* studies of biological systems to be conducted. The excitation and emission of Fluorophores are used to visualize specific structures and interactions within a system, and provide the means for analysis. Visualization of renal system structure and dynamics have be captured using IVVM, specifically ATP generation activity seen in the tubular epithelial cells and the microvascular dysfunction of blood flow associated with sepsis-induced AKI. The work proposed here focuses on using these images to quantify and explain the heterogeneity seen in the microhemodynamics of the cortical peritubular capillaries as well as mitochondrial energetics of the renal system. The information learned regarding oxygen delivery and energy consumption can be used to further understand the physio/pathophysiological interactions of the renal system in states of health and AKI.

Table of Contents

1.0 Introduction	1
1.1 Sepsis-Induced Acute Kidney Injury	3
1.1.1 Microcirculatory Dysfunction	4
1.1.2 Downregulating Metabolism Through Prioritization of Energy Consumption	5
1.2 Intravital Microscopy of the Kidney	6
1.3 Thesis Overview	9
2.0 Quantification of the Cortical Peritubular Capillary and Red Blood Cell Flow Heterogeneity in the Renal Microcirculation	14
2.1 Introduction	14
2.1.1 Image Acquisition and Description	16
2.2 Methods	18
2.2.1 Image Stabilization	18
2.2.2 Location of Peritubular Capillary Space	21
2.2.3 Estimation of Red Blood Cell Linear Density	23
2.2.3.1 Image Segmentation of Red Blood Cells	23
2.2.3.2 Assessment of Background Intensity	27
2.2.3.3 Transformation of Intensity Values to Absorption Values	29
2.3 Estimation of Red Blood Cell Velocity	32
2.3.1 Location of Red Blood Cell Centroids	33
2.3.2 Particle Tracking	33
2.4 Results	35
2.4.1 Capillary Radial Mapping	35
2.4.2 Red Blood Cell Linear Density	35
2.4.3 Red Blood Cell Velocity	35
2.5 Discussion	37

3.0 Quantification of Mitochondrial Energetics in the Kidney	43
3.1 Introduction	43
3.1.1 Image Acquisition and Description	44
3.2 Methods	45
3.2.1 Characterization of Blood Volume Space and Mitochondrial Activity .	45
3.2.2 Pixel Analysis using Geometric Ellipses	47
3.3 Results	49
3.4 Discussion	51
4.0 Summary and Future Work	53
4.1 Summary	53
4.2 Future Work	54
Bibliography	56

List of Tables

1.1	Criteria describing Acute Kidney Injury	10
1.2	Applications for multi-photon microscopy within the kidney	12
2.1	Video five metadata	20
2.2	Steps to calculate total absorption values of RBCs.	30

List of Figures

1.1	The nephron structure detailed and shown with the microcirculation.	2
1.2	Events that cause a change in blood flow in the kidney. Pathophysiological states and pharmacological events can contribute to heterogeneous and/or global reduction in renal blood flow. Ischemia invoked in the kidney will lead to AKI.	11
1.3	Visualization of the three channels that when combined create the desired image. The original image (top left) and the red (top right), green (bottom left), and blue (bottom right) channels are shown.	13
2.1	The microcirculation during sepsis-induced AKI. The capillary space (arrow) is made visible with FITC-dextran. Red blood cells (arrowhead) and the renal structure (*) are seen as silhouettes in the capillary space. The capillary space enclosed in a yellow oval is identified as region of interest (ROI) 01. The capillary space enclosed in a red box is identified as ROI 02. Scale bar = 50 μm . 17	17
2.2	Select frames from video five visually confirming blood flow heterogeneity, seen by the different red blood cell linear density in A) ROI 01 and B) ROI 02. Scale bar = 20 μm	19
2.3	Histogram analysis shows that the pixel intensity distribution becomes stretched upon applying an unsharpening filter, with capillary space becoming identifiable by its high intensity values. Histograms of A) frame 1 and B) frame 1 after applying an unsharpening filter. The contrast enhancement is seen from the difference in C) the original frame 1 and D) the stabilized contrast frame 1. Scale bar = 40 μm	22

2.4	The progression of image processing to find capillary space location. All frames were subjected to an unsharpening filter followed by an L-infinity norm analysis. The final image generated by this was binarized using Otsu's global threshold followed by a median filter. The original frame (top), result of the L-norm infinity analysis (middle), and binarized image using Otsus method (bottom). Scale bar = 40 μm	24
2.5	Image segmentation of RBCs from the capillary space. The selected frame numbers shown were chosen because they all exhibit non-overlapping RBCs. K-means clustering resulted in well-defined locations corresponding to the RBCs in the selected frames (seen in corresponding images with the blue background). Frames 4-7 are of note in how clustering was able to segment the RBCs that are in proximity of one another. Scale bar = 20 μm	25
2.6	Assessment of the background intensity. Different locations within the background were chosen to see if intensity values differed from one another. Each numerically labeled box was a location where the average intensity value was calculated.	27
2.7	Background intensity analysis of ROI 02. The average values calculated for each region, explained in Figure 2.6 with varying area are shown.	28
2.8	Frame 21 from ROI 02. The absence of RBCs in the capillary space provides an ideal estimate in how to transform the pixel intensity value to an absorption value. This absorption value better represents RBCs seen in the capillary. Scale bar = 20 μm	29
2.9	Boxplots showing the variation in total absorption values relating to the number of RBCs seen in specific frames. Simulated data was created following Table 2.2 for frames that contained more than one RBC.	31
2.10	Boxplots showing the variation in total absorption value relating to the number of RBCs seen. Red diamonds represent the average of the total absorption pertaining to each number of RBCs. A line was fit to the average total absorption values. The equation and its r^2 value are seen in the lower right hand corner.	32

2.11	Centroid location of individual RBCs within the capillary space. The first 12 frames of ROI 01 are shown, with each RBC centroid displayed with a red circle. Comparison of centroid location to original image is shown. Scale bar = 20 μm	34
2.12	Medial axis transform of the ROIs. A) (Top) The original (top left), binarized image (top right), its skeleton (bottom left), and the skeleton and edges superimposed on the ROI 01 capillary (bottom right), its medial axis transform profile (middle), and the medial axis radius (bottom). B) The same images for the ROI 02 capillary. Scale bar = 20 μm	36
2.13	Visual comparison in estimating the number of red blood cells seen in the capillary space. Results of estimating the amount of red blood cells in different image sequences highlight the heterogeneity seen in linear density and oxygen concentration present in the capillary.	41
2.14	Individual RBC velocities seen traveling through the first 100 frames of ROI 01. Each RBC that passed through the capillary was given an ID tag number. Two average velocity groups are seen: RBC tag numbers 1 to 46 and RBCs tagged 47 to 58. RBC tag numbers 1 to 46 were seen in frames one through 85, and passed through the capillary with low linear density, as opposed to RBCs tagged 47 to 58. These were seen in frames 86 through 100, and passed through the capillary with a 3 fold higher liner density as that of the previously tagged RBCs.	42
3.1	Visualization of mitochondrial function in the kidney. Multi-photon microscopy captures the A) renal microvascular space (green) and mitochondrial activity (red). The frame stamp is located in the bottom right hand corner. B) TMRM is visualised as a red color and is primarily taken up into the epithelium, which holds a high density of mitochondria. FITC-Dextran is visualized as green and resides within the vascular space.	45

3.2	Images showing the image processing steps taken to create the desired surface area sizes used to calculate average pixel channel intensities. Images shown are A) The original image, B) application of a circular mask to remove the frame time stamp, C) the outline of the surface area window, defined in size by θ , and D) the final image used to calculate the average intensity.	47
3.3	Average mitochondrial activity versus the blood volume pixel intensities. The surface area size that produced these average intensities had a θ of 60 degrees. The area was rotated 180 degrees in one degree increments. For each degree rotation, the average intensities were calculated for all frames. The color of each data point corresponds to the rotational degree that was used in calculations. A minimum volume enclosing ellipse was computed for the average pixel intensities. The parametric features of the ellipse are labeled with (x, y) being the ellipse center, a being the semi-major axis, and b being the semi-minor axis. The rotation of the ellipse (not labeled) is measured counter clockwise from the x axis.	48
3.4	The parametric features of the ellipses enclosing the average mitochondrial and blood volume intensity values for all surface area sizes. The left hand plot shows the parametric features of the ellipse where the left side y axis (black) corresponds to the values for the x center coordinate, the y center coordinate, the semi-major axis, and the semi-minor axis and the right side y axis (red) corresponds to the values for the rotation of the ellipse. The x axis is shown in log scale to highlight the change in rotation as surface area size decreases. The right hand plot shows the minimum volume enclosing ellipse (MVEE) area for the mitochondrial activity and blood volume intensity values that were calculated as different surface area windows were rotated around the center point of the images. The area increases as the semi-major and semi-minor length increase, indicating different ratios of activity to volume intensities, and an increase in spatial distribution.	50

1.0 Introduction

The kidney is a vital organ that is responsible for filtration of the blood, reabsorption of water and nutrients, regulating blood pressure, hormone production, and homeostasis of the body pH. These actions require a high energy consumption rate, making the kidney second highest in mitochondrial density and oxygen consumption. The kidneys receive approximately 1000-1200 mL/min of blood flow, equating to 20-25% of the cardiac output [44]. This high-volume flow is necessary to ensure adequate oxygen delivery and blood filtration. The afferent arterioles of the kidney supply a group of glomerular capillaries (the glomerulus), that aid in filtration of the blood. This is measured as the glomerular filtration rate (GFR). The distal ends pertaining to each glomerulus combine to form the efferent arterioles. The efferent arterioles in turn supply a second capillary network, the peritubular capillaries, which surround the renal tubules of the nephrons [44], seen in Figure 1.1. The glomerular capillary system and peritubular capillary system make up the microcirculatory system of the kidney, which is responsible for plasma filtration, electrolyte exchange, water reabsorption, and the delivery of oxygen [24].

The functional unit of the kidney is the nephron, whose total number averages between 900,000 to 1.2 million units per adult kidney. The nephron lies within the cortex and medulla regions of the kidney. The nephron interacts with the microcirculation and is divided into different segments that perform specific functions; the renal corpuscle (consisting of the glomerulus and Bowmans capsule), the proximal (convoluted) tubule, the loop of Henle, the distal (convoluted) tubule, the connecting tubule, and the collecting duct. The proximal tubule receives the filtrate from the Bowmans capsule and is responsible for the bodys reabsorption of Na^+ , HCO_3^- , Ca^{2+} , Mg^{2+} , Cl^- , K^+ , glucose, lactate, H_2O , and amino acids. High concentrations of $\text{Na}^+/\text{K}^+\text{ATPase}$ are located on the basolateral side of the epithelial cells that pump Na^+ ions into the peritubular capillaries. This is facilitated by the consumption of Adenosine triphosphate (ATP). Similarly, the distal tubules also allow reabsorption of Na^+ through $\text{Na}^+/\text{K}^+\text{ATPase}$ along with other ions including Ca^{2+} [9, 13, 21, 39, 43, 44, 47].

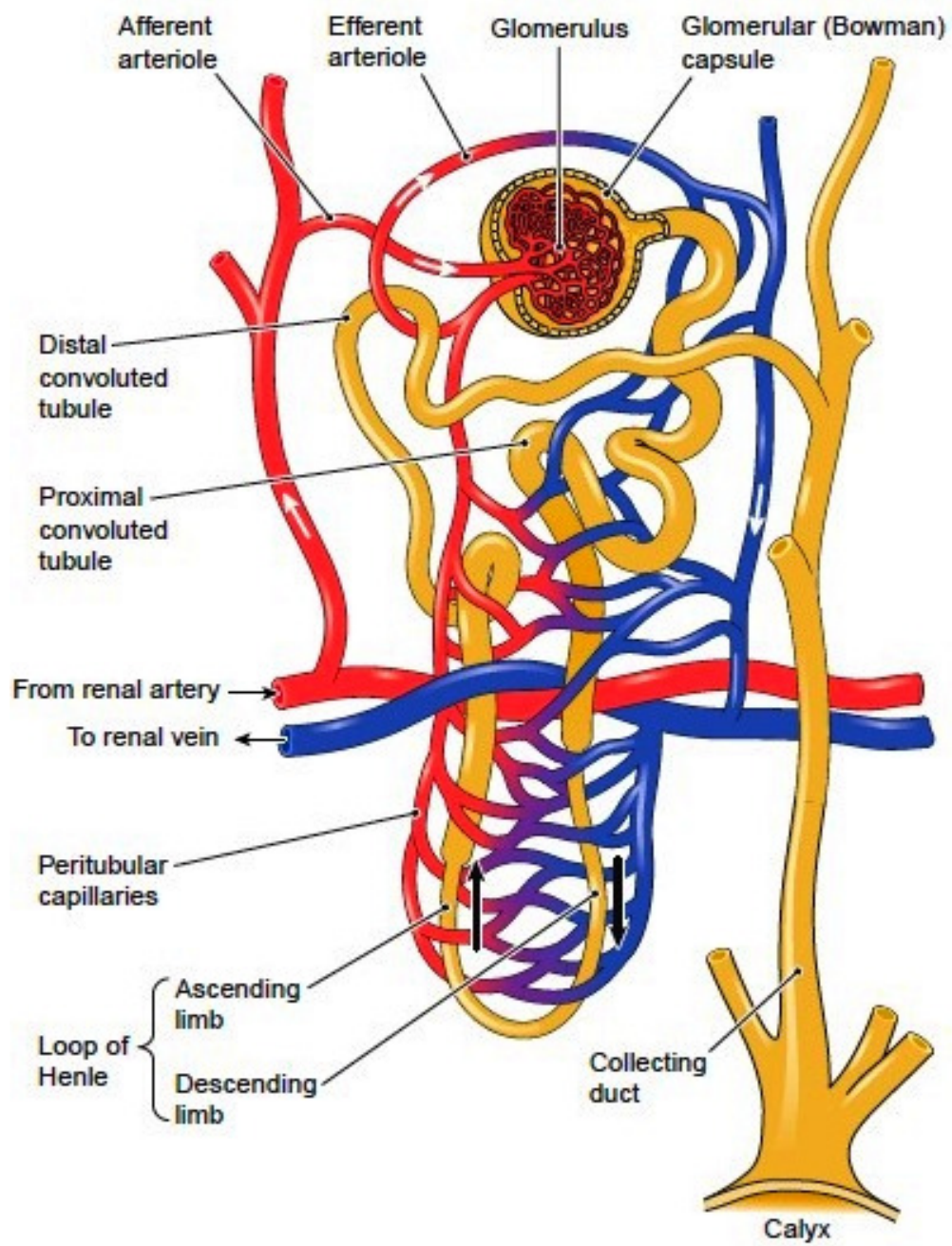


Figure 1.1: The nephron structure detailed and shown with the microcirculation.

Disruption of kidney function can be brought on by a myriad of events: physical damage to the kidney, cardiac arrest, blood loss, toxicologic effects from pharmacological drug use, and sepsis. These events introduce ischemic insult to the kidney, causing a decrease in renal functionality. This decrease in function has been given the diagnosis term of acute kidney injury (AKI). Combating AKI has led to extensive research in understanding the physiology and pathophysiology of the kidney. More recently, tools such as intravital video microscopy (IVVM) have been used to study the renal dynamics. This chapter discusses AKI, with a focus on sepsis-induced AKI, its effect on the kidney, past studies of the kidney that incorporate IVVM, and concludes with an overview of this thesis.

1.1 Sepsis-Induced Acute Kidney Injury

Acute kidney injury (formerly known as acute renal failure) is a syndrome characterized by the rapid loss of kidney function and is typically diagnosed by an increase in blood urea nitrogen (BUN) and serum creatinine, a decrease in the glomerular filtration rate (GFR), and a decrease in urine output [7, 10]. Recently, the Kidney Disease Improving Global Outcomes (KDIGO) group produced a unified version of all key criteria (Table 1.1) for classifying the stages of AKI, supplanting the previous RIFLE (Risk, Injury, Failure, Loss of kidney function, and End-stage kidney disease) and AKIN (Acute Kidney Injury Network) classifications [8].

AKI is commonly seen in hospital admissions (8-16%) [55], with ICU admission frequency ranging from 20 to 50% [18]. Of those admitted to the ICU, 50-80% succumb to in-hospital mortality [34]. AKI can be brought on as result of global or regional ischemia to the kidney [7]. The exposure of the kidney to ischemic injury can come from events detailed in Figure 1.2 [11, 14, 35]. Forward discussion will focus on sepsis-induced AKI.

Sepsis is a severe physiologic response that results from a dysregulated acute inflammatory response to infection. It is responsible for 40-50% of all AKI cases seen in critically ill patients in the ICU [22]. Proinflammatory mediators (*e.g.*, $\text{TNF}-\alpha$, Interleukin-6) are produced and recruit neutrophils to fight the pathogen, while anti-inflammatory mediators

(*e.g.*, Interleukin-10) follow, often after the pathogen levels are falling, thereby concluding the inflammatory response. Dysregulation of the inflammatory response can occur at the neutrophil recruitment stage. Neutrophils remove the pathogen but also unavoidably cause damage to surrounding healthy tissue. This damage generates further inflammation and a continued inflammatory response, which continues to cause further tissue damage, regardless if the pathogen has been eliminated. Conversely, the anti-inflammatory response may be elevated prior to complete pathogen removal, leaving the pathogen to grow and cause further damage [64]. Recent studies have shown sepsis-induced AKI can occur without ischemic injury events, with cases seeing normal or even an increased renal blood flow [22]. In fact, studies are finding similar results that show microcirculatory dysfunction, inflammation, and tubular oxidative stress are the driving physiological factors for sepsis-induced AKI [2, 17, 22, 24, 40].

1.1.1 Microcirculatory Dysfunction

The microcirculation is responsible for oxygen delivery to the kidney for tubular transport and oxidative metabolism [45]. 80% of the oxygen delivered will be used to produce ATP that will in turn will be used to drive $\text{Na}^+/\text{K}^+/\text{ATPase}$ in the proximal tubules, thick ascending limbs, and distal tubules. The high energy demand for filtration makes the microvasculature highly susceptible to areas of hypoperfusion and hypoxic injury [24, 35, 48]. A hallmark of sepsis is creating alterations in blood flow in the microvasculature. This creates heterogeneity in blood flow with an increase in the number of capillaries with deficient blood flow. These capillaries with deficient blood flow are seen having stopped flow, intermittent, and/or sluggish flow, resulting in hypoxic conditions and inadequate oxygen delivery to the surrounding renal tubular epithelial cells (TECs). Leukocytes also decrease in velocity in the microcirculation. This decrease can cause a greater time of exposure of the endothelium to these activated, cytokine secreting leukocytes and result in damage [25]. The damage done to the endothelium results in capillary leakage and interstitial fluid collection. This interstitial edema contributes to increased oxygen diffusion distances to the TECs and a decrease in microvascular flow [53]. Nitric oxide (NO) also plays a role in microcirculatory

dysfunction. Sepsis boosts the production of NO, through an increase in inducible nitric oxide synthase (iNOS). NO produced in the capillary endothelium can help regulate the vascular tone through vasodilation and control blood pressure. Even though NO production increases with sepsis, it is done so in a heterogeneous fashion in the microcirculation. This can lead to areas without means to vasodilate if necessary and thus, lead to shunting and hypoxia [22, 63].

1.1.2 Downregulating Metabolism Through Prioritization of Energy Consumption

Mitochondria are responsible for supplying the kidney its high energy demand, and are highly populated in the proximal TECs. In addition to ATP production, mitochondria also maintain intracellular calcium homeostasis, produce and control reactive oxygen species (ROS) and reactive nitrogen species (RNS) levels, and perform their own repair from injury [3, 22]. Hypoxia caused by altered flow can affect all mitochondrial functions, leading to loss of energy production to the kidney. Specifically, ROS and NO levels increase with hypoxia, and these can react and form peroxynitrite, an inhibitor of complex I and IV of mitochondria. Coupled with the release of cytochrome C from mitochondria and oxidative stress, the host cell will not maintain homeostasis and will succumb to death [3]. In scenarios such as this, the mitochondria would signal for apoptosis of the host cell, yet this is not largely viewed in the TECs of sepsis-induced AKI [22, 63]. Research points to the fact that the ETC response to injury may be attributed to reprogramming its metabolism to optimize and prioritize energy consumption, where available energy is put to functions that are required for cell survival, i.e. membrane potential, and less into high energy requiring processes such as sodium transport [22]. Mitochondria itself play a role in the protective response of TECs through mitophagy, the process of digesting and eliminating mitochondria beyond repair, and biogenesis, the rebuilding of new and healthy mitochondria. These processes are protective in that dysfunctional mitochondria are removed (decreasing ROS production), healthy mitochondria are present to facilitate low energetic functions, and proapoptotic signals are eliminated, stopping apoptosis [23].

1.2 Intravital Microscopy of the Kidney

Microscopy of living animals, called intravital microscopy, is a technique that provides a real-time *in vivo* view of functioning organs and has advanced imaging of the kidney where *in vitro* information can be supplanted with *in vivo*, allowing the quantification of distribution, behavior, and dynamic interactions of molecules to be recorded simultaneously in 3D space and time [19, 54]. IVVM is dependent on the sophistication of the microscope system and fluorescent probes (fluorophores) used. Fluorescence occurs upon the absorption of a photon by a fluorophore that moves an electron of the fluorophore to its excited state. The return of the electron to its ground state releases a photon which is detected by the system, producing an image.

Typical intravital confocal microscopy uses a single stream of photons for excitation whereas multi-photon microscopy (MPM) uses two or more low energy photons that arrive simultaneously to excite the fluorophore. MPM is desired for imaging intact organs because of the advantages it has over conventional methods. Tissue penetration is increased due to a decrease in scattering of long wavelength light. Less tissue phototoxicity is observed due to the use of lower excitation energy photons. All emitted light can be collected due to the removal of the conventional microscope pin hole. This is made possible because the probability of fluorescent excitation drops drastically as one moves away from the exact focal point, severely lowering the out of plane signal [25, 58]. These advantages have made MPM the gold standard approach for imaging processes in intact organs. Table 1.2 gives a list of areas pertaining to the kidney that can be studied using MPM [4].

Image capture is dependent on the microscope setup and can produce either greyscale or color images. Greyscale images consist of a single channel made up of pixels. Color images will consist of three separate channels, each representing the red, green, and blue contribution to the image. When combined, the 3 channels create the desired color(s). Figure 1.3 shows how the three channels make a color image when combined.

Fluorophores used in kidney studies will dictate what will be visualized. A fluorescent dye commonly used in the assessment of renal function is fluorescein isothiocyanate (FITC)-Dextran. FITC-Dextran is used routinely in cell permeability and microvasculature research.

Administration of a high weight (150-500 kDa) FITC-Dextran allows the capillaries of the renal microcirculation to be made visible upon excitation. This is because the high weight molecule (relative larger size) is not filtered by the kidney and therefore resides strictly in the capillary space and not in the tubular lumen [19]. Excitation of FITC-Dextran (along with proper image capture techniques) also allows red blood cells (RBCs) to be visualized in the capillary space as silhouettes, and therefore can also be used to observe and measure peritubular blood flow. Wu *et al.*[61] demonstrated that intermittent and stopped/no flow was present in the peritubular capillaries of mice with sepsis-induced AKI using IVVM. This was shown by using the cecal ligation and puncture (CLP) model coupled with administration of FITC-Dextran. In addition, the percentage of capillaries with continuous flow decreased over the duration of imaging of 22 hours while giving rise to intermittent and no flow.

Quantification of peritubular blood flow has been previously performed by using the “linescan” method. The rate of image capture increases as the number of scanned lines decreases. The capture of a single line running parallel in the capillary space can be recorded every 2 milliseconds [32, 41]. Stacking the line outputs results in a column of streaks running down the image, where the width is the distance of the line representing the region of interest and the height is the time span of image capture. The approximate slope of the streaks can be used to estimate the velocity [32, 41, 54]. Using this method, numerous studies have been conducted in estimating RBC velocity in the renal peritubular capillaries. Yamamoto *et al.* [62] estimated Wistar-Kyoto rat RBC velocity as $1069 \pm 146 \mu\text{m/s}$. Renal ischemia was brought on, and upon 24 hours of reperfusion, the RBC velocity was measured as $227 \pm 113 \mu\text{m/s}$. Matsumoto *et al.* [38] estimated the RBC velocity of the Sprague-Dawley rat as being $476 \pm 47 \text{ m/s}$. Molitoris *et al.* [41] estimated the normal peritubular capillary RBC velocity of the Sprague-Dawley rat as $500 \mu\text{m/s}$ (standard error not reported). Renal ischemia reperfusion via removing an arterial clamp was done, with the RBC velocity being measured at less than 100 m/s . Kang *et al.* [30] estimated the RBC velocity of the Munich-Wistar rat as $4.7 \pm 0.3 \text{ mm/s}$. Sandoval *et al.* [54] estimated rat RBC velocity of being $1462.2 \pm 86.7 \mu\text{m/s}$. Renal ischemia was brought on, and upon recovery, the RBC velocity was measured being $426.6 \pm 27.8 \mu\text{m/s}$. Holthoff *et al.* [29] were one of the few that investigated peritubular RBC velocity in sepsis-induced AKI not using the “linescan” method. They reported that

for healthy sham mice RBC velocity in continuous flowing capillaries was $370 \pm 20 \mu\text{m/s}$, while sepsis-induced AKI mice saw a reduction in RBC velocity to $126 \pm 16 \mu\text{m/s}$. These velocities were calculated by inspecting 450 capillary segments and if continuously flowing capillaries were identified, the velocity was calculated by measuring the distance traveled by a single RBC over time.

Another fluorescent dye widely used is tetramethyl rhodamine methyl ester (TMRM). TMRM is a lipophilic cationic dye. This dye accumulates in mitochondria proportional to its membrane potential $\Delta\Psi_m$. Mitochondria generate ATP by utilizing a proton electrochemical gradient potential, or electrochemical proton motive force (Δ_p), generated by the reduction of electrons through the respiratory electron transport chain. The reductive transfer of electrons through ETC protein complexes I-IV in the inner mitochondria membrane provides the energy to drive protons against their concentration gradient across the inner mitochondrial membrane (out of the mitochondrial cytoplasm) [50]. This results in a net accumulation of H^+ outside the membrane, which then flows back into the mitochondria through the ATP-generating F_1F_0 ATP-synthase (Complex V), thus producing ATP and completing the ETC. Uptake of TMRM can be measured as the intensity recorded when using MPM.

Hall *et al.* [27] studied the effects of ischemia reperfusion in rats using MPM in real time. TMRM was administered along with a ligature placed around the left renal artery. At rest, TMRM was rapidly taken up by tubular cells. TMRM intensity decreased in the proximal tubules upon ischemia via tightening of the ligature, indicating a decrease in $\Delta\Psi_m$ and ATP generation. The ability to measure mitochondrial function can be combined with other dynamics such as blood flow to give a better understanding of the renal physiology and pathophysiology. Wu *et al.* found that ROS/RNS generation in the renal tubules of sepsis-induced AKI mice was increased in areas that were bordered by capillaries with perfusion reduction [61]. This was shown by using the fluorescent dihydrorhodamine-123 (DHR). DHR is oxidized to fluorescent rhodamine by hydroxyl radical, nitrogen dioxide, peroxynitrite, and peroxidase derived species [28]. Pixel intensity fluorescence was elevated in areas that bordered capillaries with intermittent or no flow. This correlation shows that sepsis-induced AKI effects the microcirculation and mitochondrial function in a heterogeneous fashion.

1.3 Thesis Overview

This collective body of work addresses the overall oxygen content seen in the microcirculation and how this can interact with the energetics of the renal system. The structure of this body of work is as follows. Chapter 2 focuses on the cortical peritubular capillaries of the microcirculation. Image processing and analysis is performed to learn about capillary space characteristics and blood flow in sepsis-induced AKI. Capillary space diameter is investigated as well as red blood cell linear density and red blood cell velocity. These measurements give vital information regarding oxygen content available for metabolic use. Chapter 3 evaluates the energetics and the microcirculation of the renal system using MPM. Imaging results are discussed along with methods on how to quantify the relationship of mitochondrial activity and blood flow seen spatially and temporally in heterogeneous areas. The thesis concludes with Chapter 4, which presents the summary and recommendations for future work.

Table 1.1: Criteria describing Acute Kidney Injury

Stage	Serum Creatinine	Urine Output
1	1.5-1.9 times baseline	< 0.5 ml/kg for 6-12 h
	OR ≥ 0.3 mg/dl (> 26.5 μmol/l) increase	
2	2.0-2.9 times baseline	< 0.5 ml/kg for ≥ 12 h
	OR 3.0 times baseline	
3	OR Increase in serum creatinine to ≥ 4.0 mg/dl (353.6 μmol/l)	< 0.3 ml/kg for ≥ 24 h OR Anuria for ≥ 12 h
	OR Initiation of renal replacement therapy	
	OR In patients < 18 years, decrease in eGFR to < 35 ml/min per 1.73 m ²	

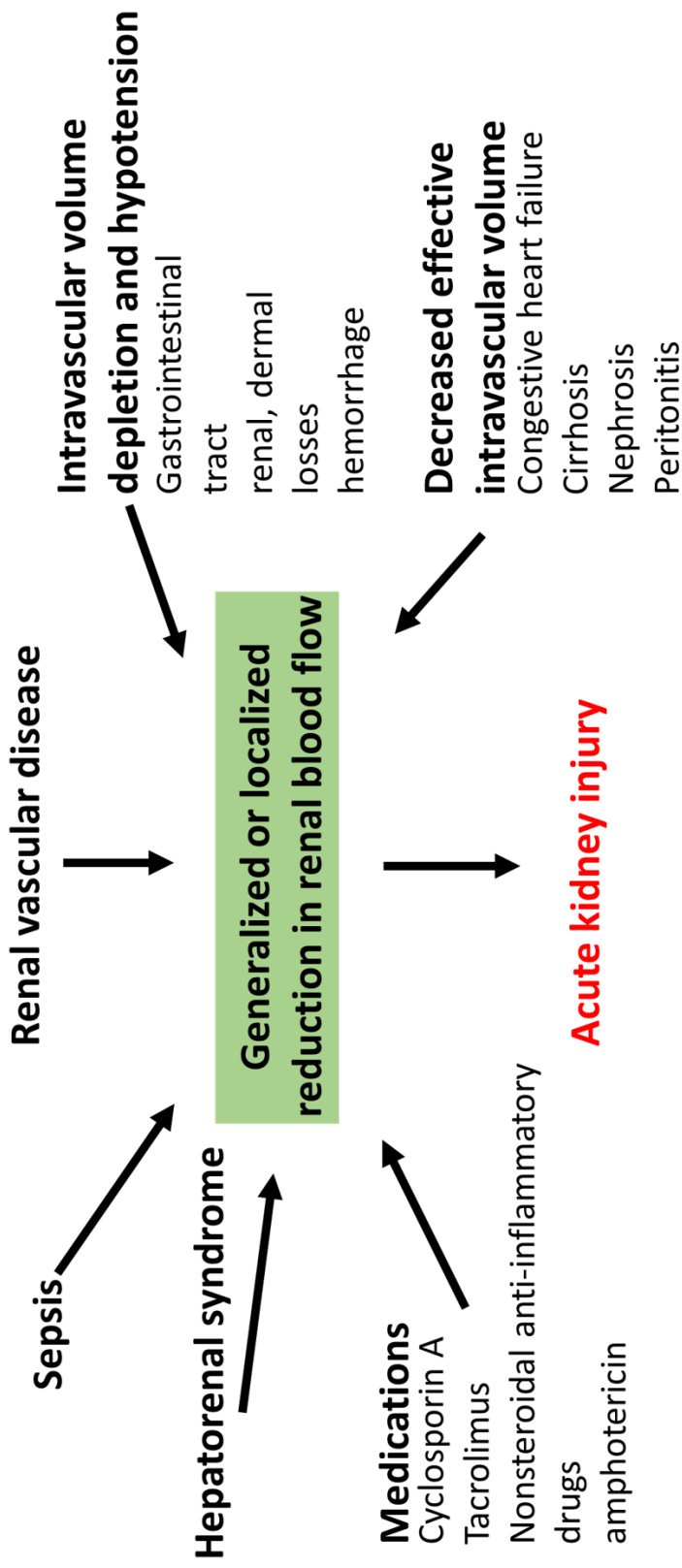


Figure 1.2: Events that cause a change in blood flow in the kidney. Pathophysiological states and pharmacological events can contribute to heterogeneous and/or global reduction in renal blood flow. Ischemia invoked in the kidney will lead to AKI.

Table 1.2: Applications for multi-photon microscopy within the kidney

Glomerular structure and function

Filtration rate
Permeability characteristics
Size/volume of glomerulus

Cell toxicity

Cell injury including necrosis or apoptosis
Surface membrane blebbing or internalization
Mitochondrial function

Cell function

Endocytosis - quantitative analysis
Intracellular trafficking and subcellular localization
Exocytosis
Metabolic State
Sites of tubular reabsorption and secretion
Ion concentrations

Microvasculature

Blood flow rate
Endothelial permeability
White blood cell adherence/rolling
Vasoconstriction



Figure 1.3: Visualization of the three channels that when combined create the desired image. The original image (top left) and the red (top right), green (bottom left), and blue (bottom right) channels are shown.

2.0 Quantification of the Cortical Peritubular Capillary and Red Blood Cell Flow Heterogeneity in the Renal Microcirculation

2.1 Introduction

The renal system becomes compromised upon injury, resulting in a decline in kidney function. This is diagnosed as acute kidney injury (AKI), with sepsis being the cause of most reported cases. Sepsis-induced AKI is complex in its pathogenesis, contributing to a dysfunctional microcirculation, an increase in reactive oxygen and nitrogen species, and the deregulation of the inflammatory system.

Intravital video microscopy (IVVM) allows the dynamics of the renal microcirculation to be visualized in real time. Of importance is the study of red blood cell (RBC) movement. As previously discussed, Wu *et al.* [61] used IVVM to show qualitatively the heterogeneity that exists in dysfunctional microcirculation and was able to categorize the peritubular capillaries that exhibited continuous, intermittent, and no flow in healthy and diseased states of the renal microcirculation in mice. RBC velocity has been evaluated as well using the line-scan method and manual evaluation of continuously flowing red blood cells [29, 41]. The study of RBC linear density and of the peritubular capillaries is notably absent when pertaining to the change in size brought on by vasodilation or vasoconstriction via injury.

The wealth of information that IVVM provides can be analyzed using computer vision. A challenge in computer vision, the field of extracting information from images or movies, is creating methods that allow a computer to see what the human eye sees. To accomplish this, processing techniques such as filtering and segmentation can be applied to images to give an enhancement of features that can aid a computer in what to look for in an image. Filtering uses a neighborhood of pixels in a convolution mask or kernel, to transform the intensity of pixels into an image. Kernels are typically rectangular by application and odd numbered in rows and columns, allowing assignment of a central pixel within the kernel. Different filtering methods result in different intensity outputs of the image. Smoothing filters reduce image noise, via assigning an overall average value to the pixel of interest

based on the kernel. Of these, a blurring filter takes the average of the kernel and applies it to the pixel of interest while a Gaussian filter uses a weighted average of intensity values from nearby pixels and applies it to the pixel of interest, where this weight is based on a Gaussian distribution. Conversely, median filters reduce “salt and pepper noise” by assigning the median value of neighboring pixels to a pixel of interest. Filters can be combined to achieve image enhancement as well. An unsharpening filter involves subtracting a blurred image $f_{b(x,y)}$ from the original image $f_{(x,y)}$, then adding a weighted result $g_{(x,y)}$ of that image to the original. This returns the unsharpened image $f_{unsharp(x,y)}$, whose features show an enhancement of contrast in the image. Another type of filter, the bilateral filter, is a nonlinear, edge-preserving and noise-reducing smoothing filter. The intensity value at each pixel in an image is replaced by a weighted average of intensity values from nearby pixels. This weight is based on a Gaussian distribution. Crucially, the weights depend not only on the Euclidean distance of pixels, but also on the radiometric differences. This preserves sharp edges by looping through each pixel and adjusting the weights to the adjacent neighboring pixels [60].

Image segmentation partitions pixels into homogeneous clusters, giving an image a more meaningful representation of structures within it. The simplest thresholding approach is grey level thresholding, where objects and background are separated based on an intensity threshold value. Global thresholding is based on the assumption that the image has a bimodal histogram where the foreground object can be extracted from the background. Otsu’s method of global thresholding is commonly utilized in such a case, where a threshold is selected for separation based on the minimization of within-class variance. Regions of high homogeneity will exhibit low variance, thus separating the foreground and background pixels into their respected groups [51].

This chapter focuses on the use of image processing to describe the characteristics of the cortical peritubular capillaries and to mathematically model the quantification of red blood cell movement from images of the renal microcirculation *in vivo*. Our goal is to better understand how the renal microcirculation is heterogeneously dispersed as it pertains to the dynamics of oxygen delivery to the surrounding tubular epithelial cells (TECs). An image processing pipeline was developed to calculate capillary diameter and RBC movement. The

pipeline was developed using ImageJ software [56] and in Python version 3.6, with prominent use of scikit-image [60], openCV [12], and trackpy [1] libraries. Following image acquisition, unwanted movement on a per frame basis of the renal microcirculation videos was stabilized to more accurately locate positions of RBCs and capillary space. Next, regions of interest were chosen within the image sequence for analysis. The location of the capillary space and individual red blood cells was found, allowing capillary radius and RBC velocity to be calculated. Methods to estimate RBC linear density in the capillaries were developed for situations where individual RBCs could not or cannot be identified. The results presented show a means to map the heterogeneity seen within each capillary as well the capillaries captured in the images. Discussion pertaining to how this can aid mathematical modeling of oxygen delivery in the renal microcirculation and therapeutic evaluation concludes this section.

2.1.1 Image Acquisition and Description

Images *in vivo* of the renal microcirculation were collected using IVVM from a C57BL/6J mouse with sepsis-induced AKI from cecal-ligation and puncture (CLP). A high weight FITC-Dextran was administered to the mouse via tail vein injection and resided within the capillary space. An inverted confocal microscope equipped with a digitizing camera was used to collect the images. Images were acquired through Dr. Hernando Gomez of UPMC, Department of Critical Care Medicine and Center of Critical Care Nephrology. 17 videos of the microcirculation were recorded and labeled, with video five being selected for initial video processing and analysis. Video five was chosen after visual inspection revealed a heterogeneity in blood flow. This was expressed as continuous, intermittent, or stopped/no flow in the capillaries, the hallmark signs of microcirculatory dysfunction from sepsis. Two capillary regions of interest (ROIs) within video five were selected for image processing and analysis, shown in Figure 2.1.

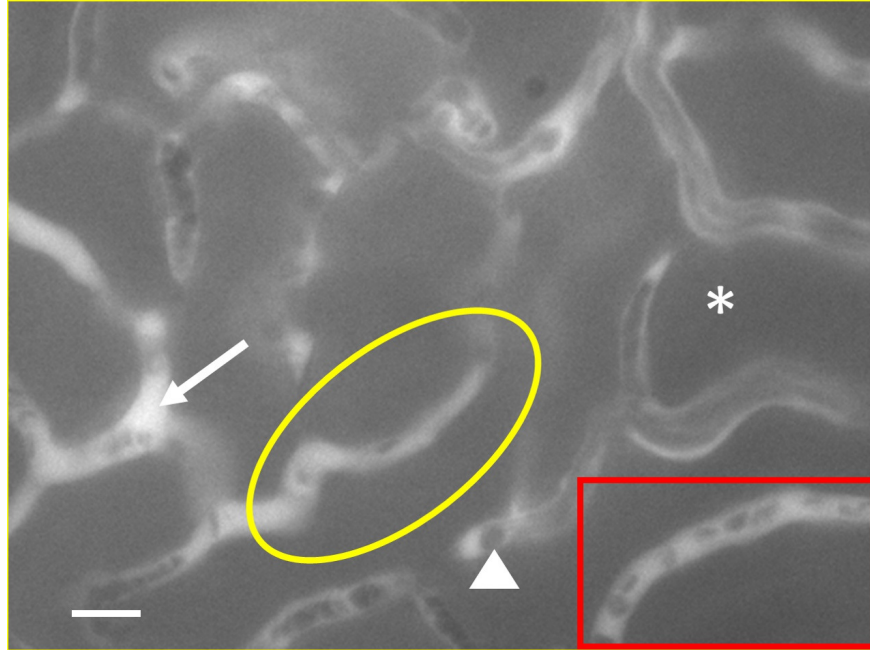


Figure 2.1: The microcirculation during sepsis-induced AKI. The capillary space (arrow) is made visible with FITC-dextran. Red blood cells (arrowhead) and the renal structure (*) are seen as silhouettes in the capillary space. The capillary space enclosed in a yellow oval is identified as region of interest (ROI) 01. The capillary space enclosed in a red box is identified as ROI 02. Scale bar = 50 μm .

These two ROIs, labeled ROI 01 (the yellow oval), and ROI 02 (the red box), were selected because of their blood flow heterogeneity seen in the vascular space over time. Figure 2.2 shows a selection of frames from ROI 01 and ROI 02 highlighting the heterogeneity of blood flow within the capillaries. Metadata pertaining to video five is described in Table 2.1.

2.2 Methods

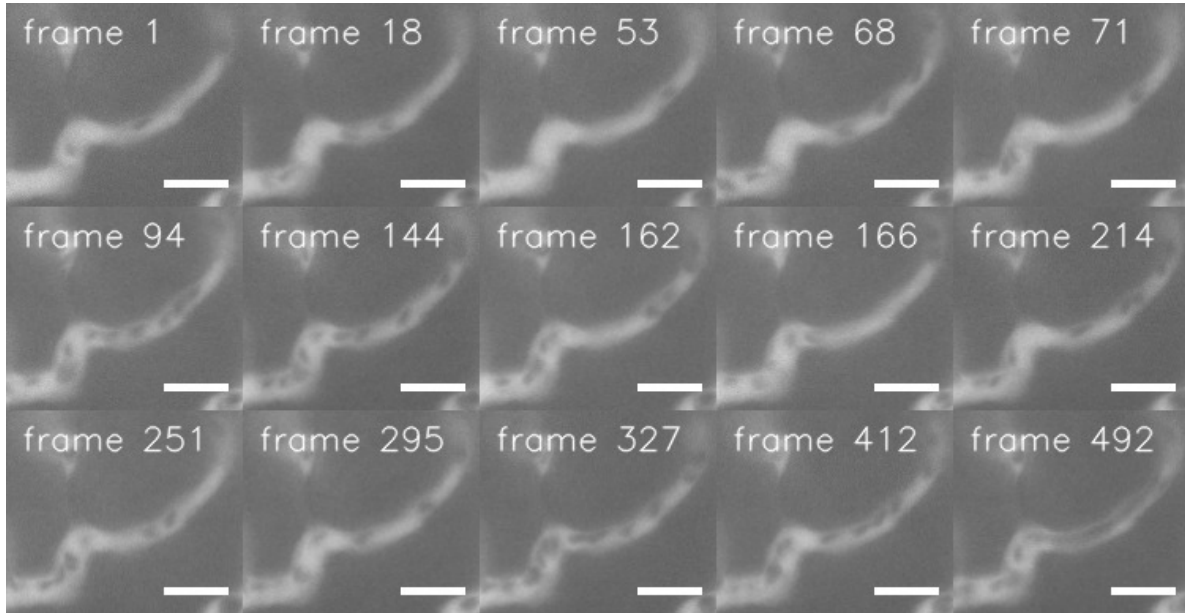
Accurate identification of the peritubular capillary space requires image stabilization and the means to differentiate the capillaries from the renal structures. Once located, analysis of the capillaries can be conducted, primarily determining the medial axis radius along a capillary length. Having the location of the capillary space allows the means to locate RBCs, their characteristics, their quantity in a capillary, and their velocity.

2.2.1 Image Stabilization

The videos received from the experiment possessed an inherent jitter due to the pulsation of the heart and respiration of the mouse. This movement caused distortion and disconnected the pixel locations of the capillary space from one another on a frame by frame basis. To correct this, the Lucas-Kanade algorithm [5] was used to stabilize the image sequence. This algorithm aligns a template image $T(\mathbf{x})$ to an input image $I(\mathbf{x})$, where $\mathbf{x}=(x,y)^T$ is a column vector containing the pixel coordinates. First, let $\mathbf{W}(\mathbf{x};\mathbf{p})$ be the parameterized set of allowed warps, where $\mathbf{p} = (p_1, \dots, p_n)^T$ is a vector of parameters. The warp $\mathbf{W}(\mathbf{x};\mathbf{p})$ takes the pixel $\mathbf{W}(\mathbf{x};\mathbf{p})$ in the coordinate frame of the template T and maps it to the sub-pixel location $\mathbf{W}(\mathbf{x};\mathbf{p})$ in the coordinate frame of the image I . The goal of the Lucas-Kanade algorithm is to minimize the sum of squared error between the template image T and the image I warped back onto the coordinate frame of the template:

$$\min \sum_x [I(\mathbf{W}(\mathbf{x};\mathbf{p})) - T(\mathbf{x})]^2 \tag{2.1}$$

A



B

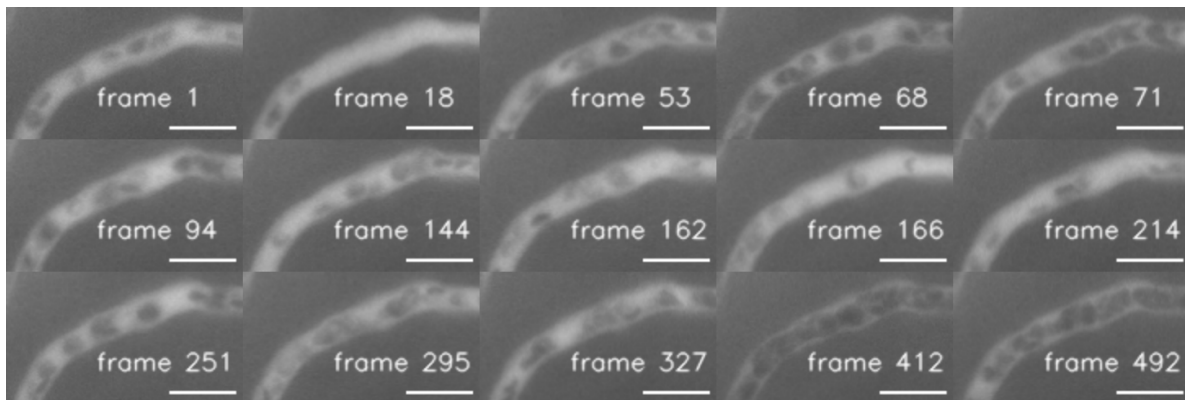


Figure 2.2: Select frames from video five visually confirming blood flow heterogeneity, seen by the different red blood cell linear density in A) ROI 01 and B) ROI 02. Scale bar = 20 μm .

Table 2.1: Video five metadata

Description	Units	Value
Width	μm	224.46
Width	pixels	464
Height	μm	167.37
Height	pixels	346
Size	megabytes	162
Resolution	pixels per μm	2.0672
Video length	seconds	26.35
Number of frames	N/A	527
Frames per second	N/A	20

The Lucas-Kanade algorithm uses the assumption that a current estimate of \mathbf{p} is known and then iteratively solves for changes to the parameters $\Delta\mathbf{p}$, which can be shown as

$$\min_x \sum_x [I(\mathbf{W}(\mathbf{x}; \mathbf{p}) + \Delta\mathbf{p}) - T(\mathbf{x})]^2 \quad (2.2)$$

Equation (2.2) is approximately minimized with respect to $\Delta\mathbf{p}$, which is used to update the parameter set

$$\mathbf{p} \leftarrow \mathbf{p} + \Delta\mathbf{p} \quad (2.3)$$

Iteration of Equations 2.2 and 2.3 occur until the estimates of the parameters \mathbf{p} converge. The test for convergence is done by evaluating if the norm of the vector $\Delta\mathbf{p}$ is below a defined threshold level ϵ , $\|\Delta\mathbf{p}\| \leq \epsilon$. The Lucas-Kanade algorithm was applied to video five using ImageJ and the Image Stabilizer plugin [31]. The first frame of the video was used as the template for template matching. The edges of the stabilized videos were cropped to remove noise introduced by the stabilization.

2.2.2 Location of Peritubular Capillary Space

The greyscale intensity values assigned to each pixel of the images was reduced from 16 bit to 8 bit, ranging now from a value of 0 to 255, where an intensity value of zero is black and an intensity value of 255 is white. Visually, one can see from Figure 2.1 that pixels representing the capillary space void of particles are of higher intensity values than that of the renal structure and red blood cells. Figure 2.3A shows a histogram of the pixel intensity values of frame 1.

The distribution of intensity values makes it difficult to locate a definitive value or value range to assign to pixels that represent the capillary space. An increase in contrast alleviates this problem by making the capillary space distinguishable from the rest of the image. This is done by subjecting the images to an unsharpening mask filter, implemented in ImageJ [8]. Figure 2.3B shows a histogram of the pixel intensity values of frame 1 after the unsharpening mask has been applied. It can be seen that a large increase in pixels with high intensity occurred due to the unsharpening mask. These high intensity pixels give a better representation of where the capillary space is in the image. Figure 2.3(C,D) shows the difference in appearance between frame 1 before and after the unsharpening mask filter was applied. This technique also enhances the contrast and difference in pixel intensity between the red blood cells and the capillary space. This creates a more defined edge between the capillary space and epithelial tissue boundary as well as the edges between the capillary space and RBCs. Moving forward, the images that have undergone stabilization and unsharpening will be defined as stabilized contrast images.

The stabilized contrast images were evaluated with an L-infinity norm described by:

$$\|I_{(i,j)}\|_{\infty} = \max(|I_{k(i,j)}|) \forall k \in \{1, 2, \dots, p\}; \forall i \in \{1, 2, \dots, m\}; \forall j \in \{1, 2, \dots, n\} \quad (2.4)$$

Here I is the intensity, m equals the number of pixels in the x direction, n equals the number of pixels in the y direction, and p equals the number of frames in a video. This calculates the highest intensity value on a per pixel basis, pertaining to that pixel location, over all frames. The image created by Equation (2.4) can be seen in Figure 2.4 (middle).

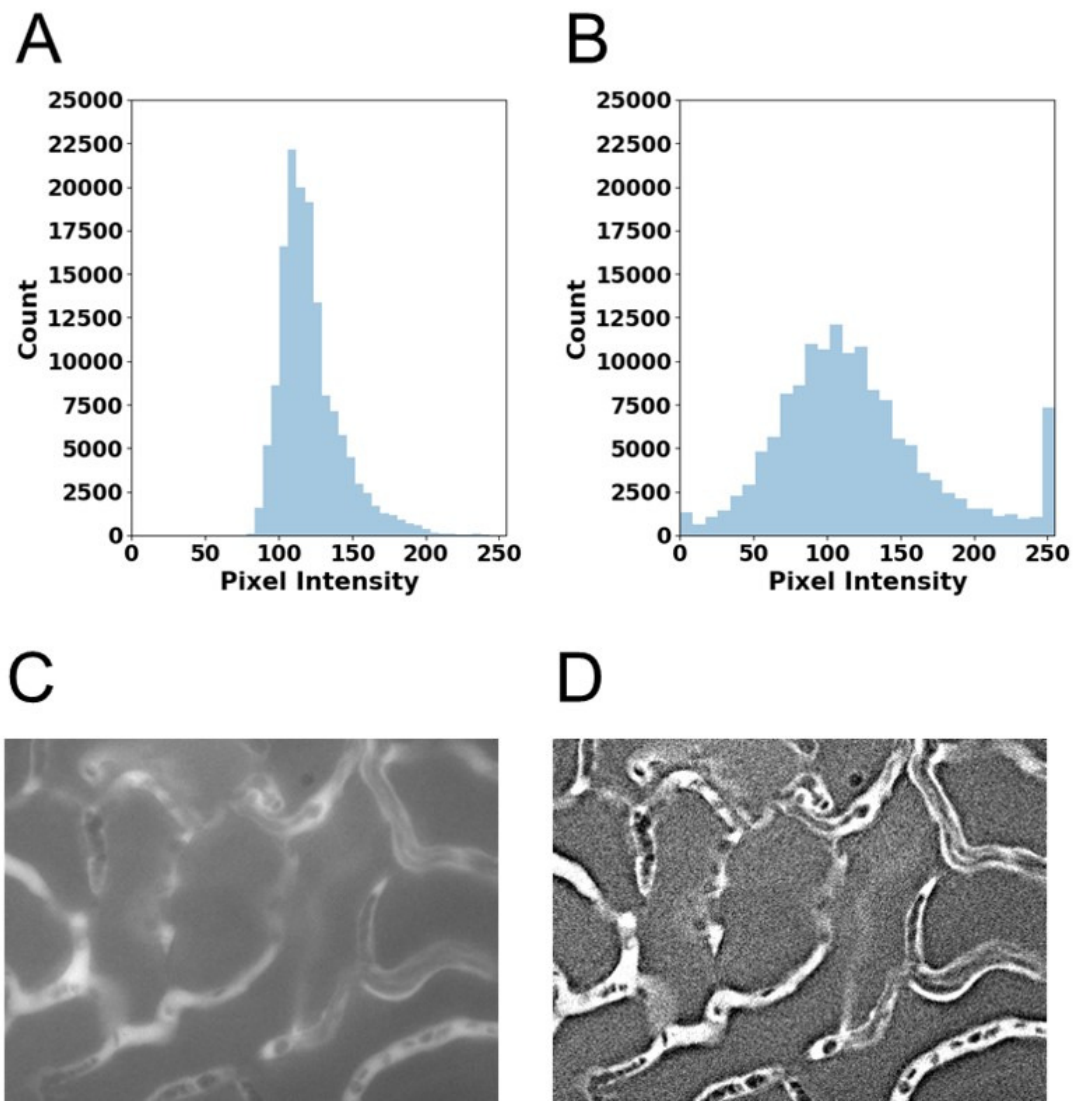


Figure 2.3: Histogram analysis shows that the pixel intensity distribution becomes stretched upon applying an unsharpening filter, with capillary space becoming identifiable by its high intensity values. Histograms of A) frame 1 and B) frame 1 after applying an unsharpening filter. The contrast enhancement is seen from the difference in C) the original frame 1 and D) the stabilized contrast frame 1. Scale bar = 40 μm .

The left hand side of Equation (2.4) was binarized using Otsu's global thresholding. Otsu's threshold was chosen as we are locating the capillary space as a foreground/background

problem, where the capillaries are the foreground and all other structures are the background. A median filter was applied to the thresholded image to eliminate spurious pixels that were mistakenly identified as the foreground. The final binarized image of the capillary space is viewed in Figure 2.4 (bottom). With this image, all pixel locations pertaining to the white pixels are now known.

2.2.3 Estimation of Red Blood Cell Linear Density

The density of RBCs within the microcirculation can describe the concentration of oxygen available for use in cellular metabolism. It has been shown using IVVM that blood flow exhibits instances of low and of high linear density. In both cases, RBCs can crowd, overlap, and surpass one another as they flow through a capillary. This presents a challenge in how to accurately assess how many RBCs pass through an arbitrary capillary length at a given time. A mathematical model estimating the number of RBCs seen in an arbitrary space was developed based on data collected pertaining to various RBCs identified in a series of frames.

2.2.3.1 Image Segmentation of Red Blood Cells Estimation of the number of RBCs seen requires information as to what the RBCs look like in the capillary space. Figure 2.5 shows frames selected to help describe how individual RBCs are portrayed. These frames will be given the name selected frames when discussed or referenced. Each frame in the selected frames set contains a predefined number of RBCs that were visually non-overlapping with one another.

Segmentation of the RBCs was done by taking a foreground/background segmentation approach, where the RBCs were the foreground and the capillary space was the background. The method presented by Crocker and Grier [15] was used for locating the RBCs. Originally presented as a means for colloidal suspension particle tracking, Crocker and Grier's method can be applied to a wide range of particle finding studies. Colloidal suspension particles, when imaged, can be explained as Gaussian distributed 2-dimensional spheres, where the pixel centroid of the particle has the highest intensity. The pixel intensity of the particle then

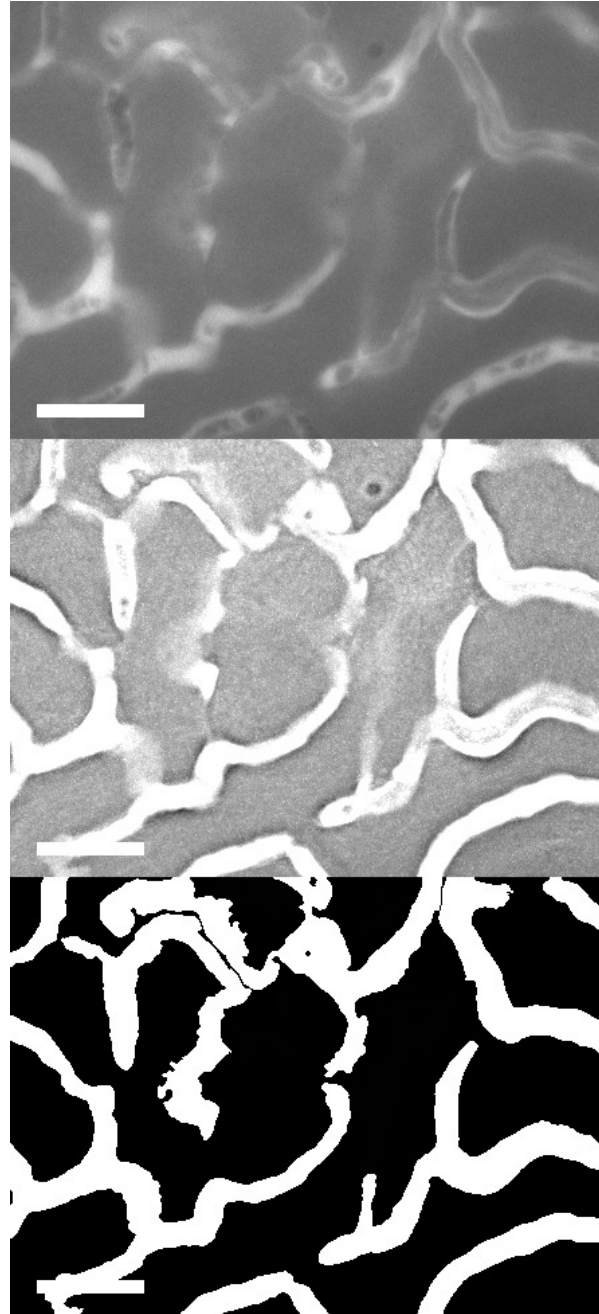


Figure 2.4: The progression of image processing to find capillary space location. All frames were subjected to an unsharpening filter followed by an L-infinity norm analysis. The final image generated by this was binarized using Otsu's global threshold followed by a median filter. The original frame (top), result of the L-norm infinity analysis (middle), and binarized image using Otsus method (bottom). Scale bar = 40 μm .

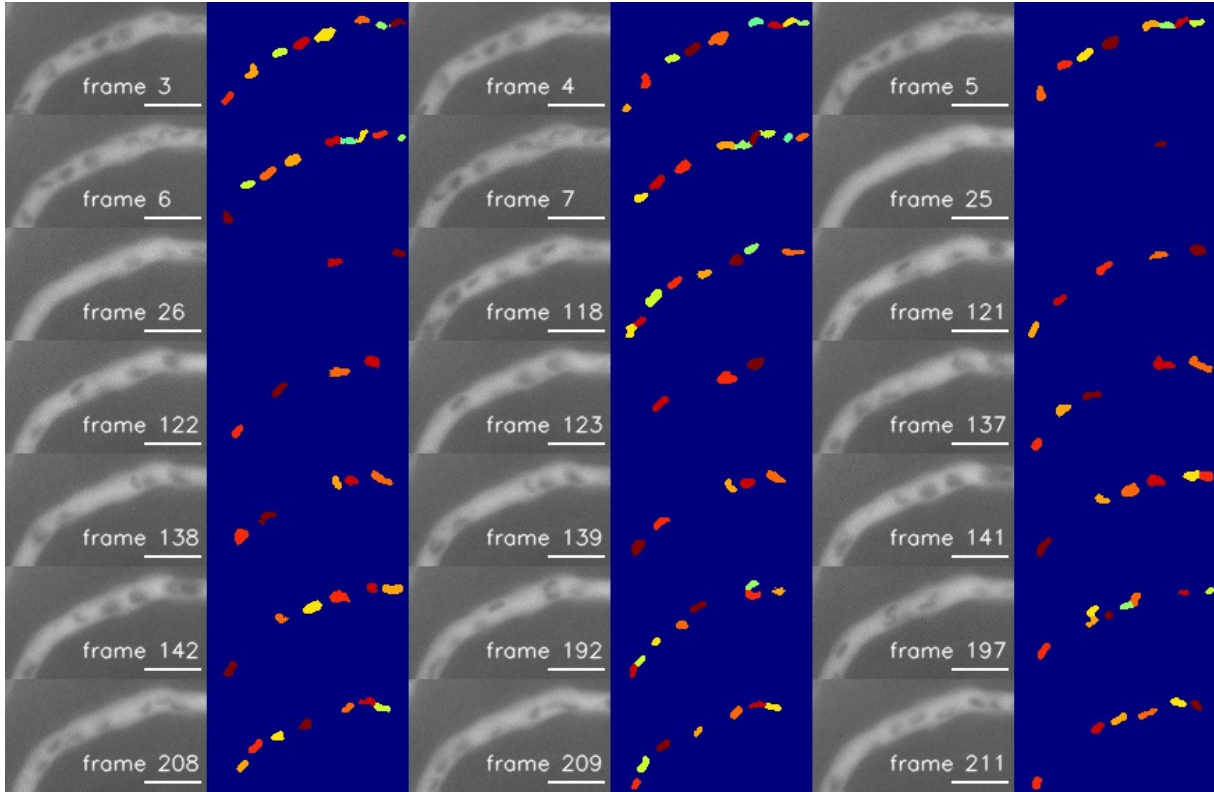


Figure 2.5: Image segmentation of RBCs from the capillary space. The selected frame numbers shown were chosen because they all exhibit non-overlapping RBCs. K-means clustering resulted in well-defined locations corresponding to the RBCs in the selected frames (seen in corresponding images with the blue background). Frames 4-7 are of note in how clustering was able to segment the RBCs that are in proximity of one another. Scale bar = 20 μm .

decreases as you move radially out towards the edge. The stabilized microcirculatory images were pre-processed using a bilateral filter and inverted to give the RBCs an appearance more representative of the particles described by Crocker and Grier. Once pre-processed, the algorithm was implemented.

The algorithm is as follows:

1. Apply a blurring average filter to the image.
2. Apply a Gaussian filter to the original image.

3. Subtract the blurred average image from the Gaussian filtered image. Background features and imperfections will have been removed leaving an image with ideal estimates of the features belonging to the particles (RBCs).
4. Identify local brightness maxima within the image as potential particle centroids. A threshold is used as a cutoff for accepting a brightness maxima value.
5. Refine local estimates. Calculate the offset (ϵ_x, ϵ_y) from the pixel at (x,y) found in step 4 to the brightness-weighted centroid of the pixels in a region around (x,y) . The centroid of the particle is defined as $(x_0, y_0) = (x + \epsilon_x, y + \epsilon_y)$. If $|\epsilon_x|$ or $|\epsilon_y|$ exceeds more than 0.5, the pixel is moved and refinement is recalculated. If not, (x,y) is recorded as the particle centroid.

Steps 1-3 of The Crocker and Grier algorithm was performed on each selected frame to produce an ideal estimate image of the foreground RBCs from the background capillary space. This separated the individual RBC pixels from the empty capillary space pixels. This was accomplished with Trackpy [1], a Python open-source software package. The contours of each RBC in each frame were found using the scikit-image function *findcontours* in Python. The contours provided the pixel coordinates needed to analyze the surface area intensity of each RBC. From the contours, the total and average pixel intensity of each individual RBC was calculated.

In some instances, contour mapping enclosed multiple RBCs due to the proximity of one to another, altering the true number of RBCs that are seen. This was alleviated by introducing a k-means clustering of the RBC pixels. The k-means algorithm searches for a pre-determined number of clusters within an unlabeled dataset. This is done by first assigning each observation to a cluster center or centroid. The Euclidean distance between each observation and centroid is calculated. Next, the mean of the observations with the minimum Euclidean distances from its pre-existing centroid is calculated. This mean is used to update the centroid. This process is iterated until the assignment of centroids does not change. Knowing the true number of RBCs in each frame, the k-means algorithm was implemented using the scikit-learn *kmeans* function in Python [49]. Clustering resulted in 129 individual RBCs and can be seen in Figure 2.5.

2.2.3.2 Assessment of Background Intensity Image capture can lead to unwanted intensities due to camera placement, camera exposure, or inherent noise. This can distort the image and create biased intensity outputs. Assessment of the background intensity can be done to see if any areas are a result of poor image development. The renal lumen in the frames should all have the same relative intensity output and can be deemed the background intensity value. Average intensities of different locations of the lumen were calculated over all frames to see if the values differed from one another. Figure 2.6 shows the location of where the average intensities were calculated.

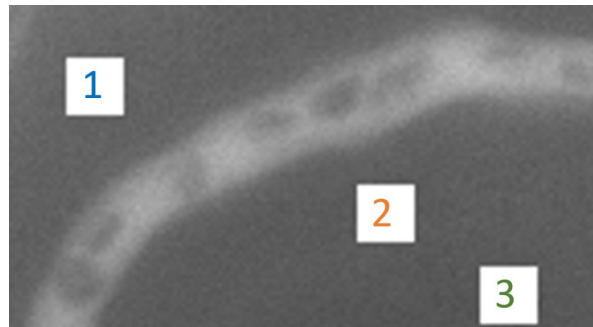


Figure 2.6: Assessment of the background intensity. Different locations within the background were chosen to see if intensity values differed from one another. Each numerically labeled box was a location where the average intensity value was calculated.

The area of the square regions ranged from 25 to 169 pixels to see if an expansion in pixel area altered the results. All frames were subjected to this analysis, with the results shown in Figure 2.7.

The average intensities seen from regions 2 and 3 are similar to one another, while region 1 demonstrates a higher average intensity. This difference could indeed change image analysis based on image location. Interestingly, the average intensity values of all regions exhibit similar profiles. Correlation analysis showed that all regions showed strong correlation with one another. Knowing this, a correction factor was created to account for any background intensity influencing the capillary space. The average intensity of the 81 square pixels from region 1 and region 2 were averaged for each frame to create the correction factor. This was calculated to correct for any background intensity influencing the capillary space. All

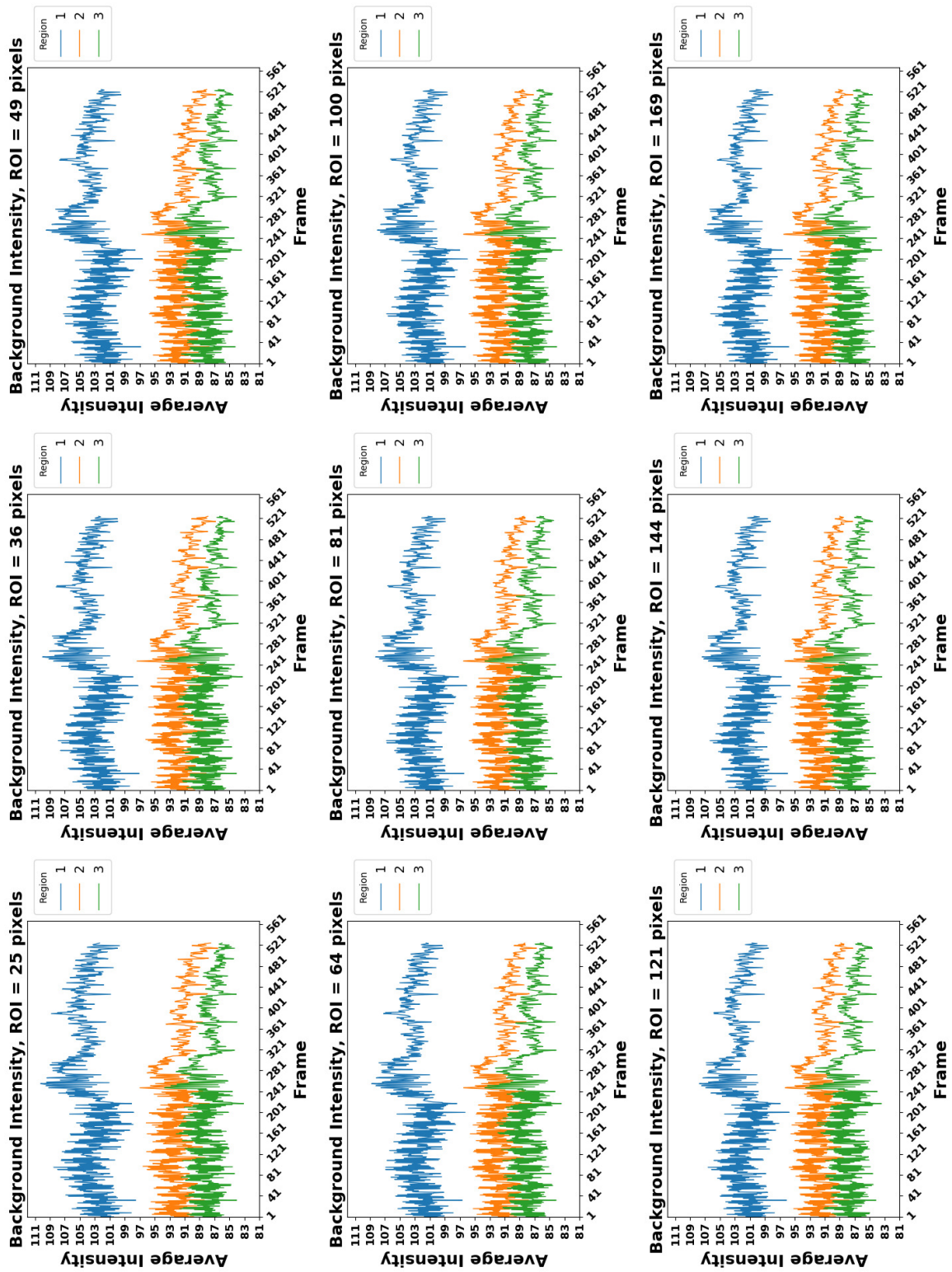


Figure 2.7: Background intensity analysis of ROI 02. The average values calculated for each region, explained in Figure 2.6 with varying area are shown.

averaged data points were divided by the first averaged data point and multiplied with their corresponding frames. This approach alleviated the influence of background intensity on the capillary space and RBCs.

2.2.3.3 Transformation of Intensity Values to Absorption Values Red blood cells are assigned a lower intensity value when compared to the capillary space, as a result of the experimental setup and use of FITC-Dextran. Accordingly, individual RBCs have a higher intensity value when compared to RBCs that overlap with one another. To have the data, *i.e.* the RBCs, increase in value from single to overlapped RBCs, pixel intensity was transformed to represent what has been termed “absorption” values. The highest intensity values represent the void capillary space. The assumption can be made that these pixels represent the baseline, corresponding to an absorption value of zero. Frame 21, seen in Figure 2.8, provides excellent viewing of the void capillary space, completely empty of RBCs and other solutes. Averaging the values of the empty capillary space pixels results in an average intensity value of 174. This value was used to transform the intensity value to an absorption value. This is done by subtracting a pixel intensity from 174. With this approach, overlapping RBCs are represented with a higher pixel value than that of individual RBCs.

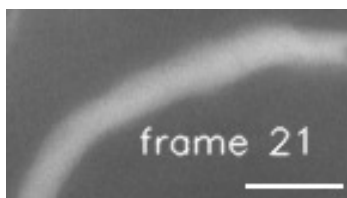


Figure 2.8: Frame 21 from ROI 02. The absence of RBCs in the capillary space provides an ideal estimate in how to transform the pixel intensity value to an absorption value. This absorption value better represents RBCs seen in the capillary. Scale bar = 20 μm .

The relationship between a known number of RBCs and their total pixel absorption level was explored. This was done to have a better understanding of how multiple RBCs are represented on an absorption value basis. Boxplots were created to show the variation in assigning an absorption value to a known number of RBCs specific to the selected frames. A

combination method of calculating the absorption of a specific number of RBCs pertaining to each frame was used to ensure sufficient data collection. For each frame that had more than 1 RBC, all combinations of $(N - 1)$ RBCs are evaluated for absorption. This method is outlined in Table 2.2.

Table 2.2: Steps to calculate total absorption values of RBCs.

1	FOR each selected frame
2	perform segmentation of RBCs
3	FOR number of segmented RBCs
4	IF number greater than 1
5	select (number - 1) RBC(s)
6	calculate total pixel absorption of the number of segmented RBC(s)
7	repeat number times by removing each RBC once
8	ELSE
9	calculate total pixel absorption of the number of segmented RBC(s)
10	END

Boxplots showing the variation in assigning an absorption value to a known number of RBCs specific to the selected frames is shown in Figure 2.9. This showed a general linear increase in total absorption as the number of RBCs present in the frame increased. To further examine this, boxplots of total absorption values corresponding to a number of RBCs regardless of frame were plotted, as seen in Figure 2.10. A clear linear relationship was seen between absorption value and number of RBCs. A line was fit to the average absorption value, giving the equation

$$y = 2040.25x - 90.37 \tag{2.5}$$

where y equals the total absorption and x equals the number of RBCs.

Equation (2.5) shows a negative y intercept, a value realistically not possible, as the absorption value of zero RBCs should be zero. The assumption to neglect the y -intercept

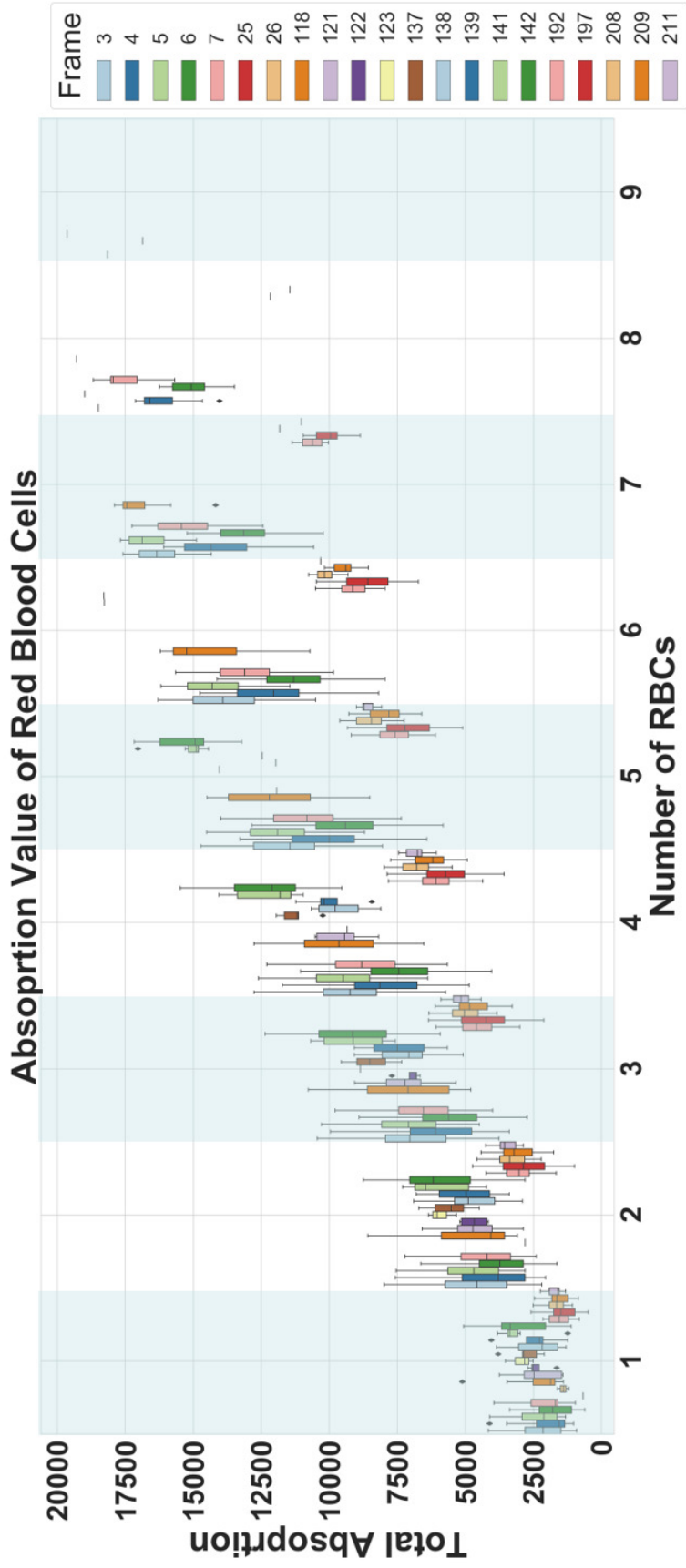


Figure 2.9: Boxplots showing the variation in total absorption values relating to the number of RBCs seen in specific frames. Simulated data was created following Table 2.2 for frames that contained more than one RBC.

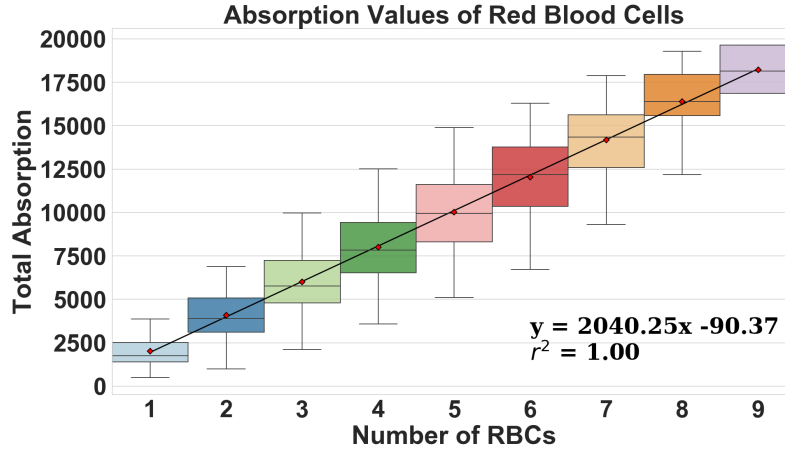


Figure 2.10: Boxplots showing the variation in total absorption value relating to the number of RBCs seen. Red diamonds represent the average of the total absorption pertaining to each number of RBCs. A line was fit to the average total absorption values. The equation and its r^2 value are seen in the lower right hand corner.

was justified given the fact that the absorption value for one RBC resides around 2000. Equation (2.5) now can be used as a model to estimate the number of RBCs present given a total absorption value.

2.3 Estimation of Red Blood Cell Velocity

Quantification of red blood cell velocity can provide a means to measure blood flow and the amount of oxygen transport seen within the capillaries. Blood flow within the renal microcirculation can change with AKI, resulting in a change in oxygen delivery to the surrounding cells. Understanding this quantitative change in the availability of oxygen for cellular metabolism can therefore help in explaining kidney function seen in AKI. Continuous blood flow within the described ROIs was analyzed to determine RBC velocity. It was determined that locating RBCs in continuous flow within the capillary space could be presented

as a foreground/background segmentation problem, with the RBCs being the foreground and the empty capillary space being the background. Once located, the tracking of the RBCs through the capillary was performed to estimate their velocity.

2.3.1 Location of Red Blood Cell Centroids

Individual RBC centroid coordinates within the images were obtained as the initial step in calculating the velocity of the blood. Similar to the method outlined in section 2.2.3.1, a thresholding approach of segregating the foreground (RBCs) from the background (the capillary space) was taken. The full algorithm (steps 1-5, see section 2.2.3.1) presented by Crocker and Grier [15] was used for locating the RBC centroids. The Trackpy [1] package was used to find the centroids of the RBCs of the first 100 frames of ROI 01. Centroid coordinates were only recorded if they were found inside the capillary space. Manual inspection of ROI 01 was performed to remove any false centroid labeling or to add any centroids that were not labeled. Figure 2.11 shows the first 12 frames of ROI 01 with red circles superimposed on where centroids were located as a demonstration of performing RBC location.

2.3.2 Particle Tracking

All RBC centroids were assigned a pixel location corresponding to a point on the ROI 01 medial axis skeleton (see section 2.4.1) on a per frame basis. The reason for assigning RBC centroids to skeletal coordinates is to minimize error in measuring the potential distance a RBC travels in sequential frames. For example, the line point measurement between two frames may take a trajectory outside the capillary space, creating a false representation of movement. Measuring the distance traveled along the medial axis skeleton circumvents this. Centroid assignment was done by calculating the Euclidean distance between each RBC centroid and each medial axis skeleton pixel coordinate. The medial axis coordinate corresponding to the minimum Euclidean distance from the centroid was assigned a 1 to represent a centroid while the other coordinates were assigned a zero. This mapping was created as a means to organize centroid location(s) pertaining to each frame and to be used to efficiently link RBC movement from one frame to the next.

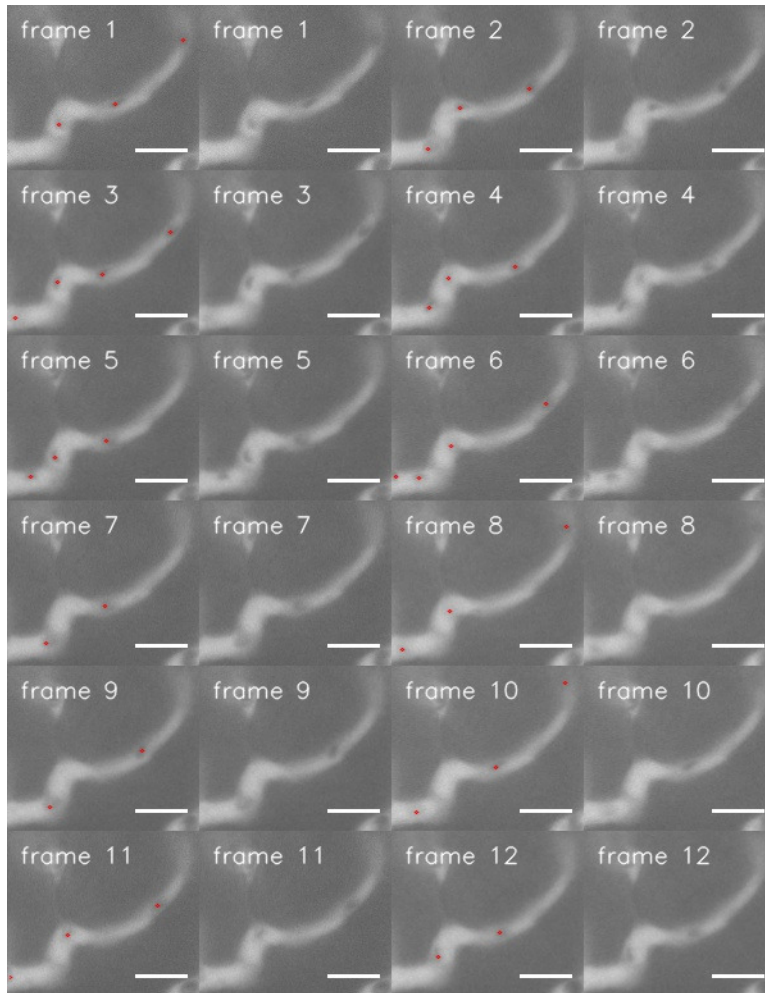


Figure 2.11: Centroid location of individual RBCs within the capillary space. The first 12 frames of ROI 01 are shown, with each RBC centroid displayed with a red circle. Comparison of centroid location to original image is shown. Scale bar = $20 \mu\text{m}$.

Semi autonomous particle tracking was applied to link RBC movement seen on a frame by frame basis. Determination of the RBCs that entered and left the capillary on a frame by frame basis was incorporated to ensure accurate linking. A maximum limit of potential movement was also incorporated to further increase the accuracy in measurement. RBCs were linked by using the particle's pixel location coordinates. These instantaneous velocities were then evaluated to determine multiple frame trajectories. Linking the RBC movements

over the frames pertaining to each identified RBC created averages of RBC velocity through the entire capillary, represented as the mean \pm the standard error of mean (s.e.m.).

2.4 Results

2.4.1 Capillary Radial Mapping

A medial axis transform was used to calculate the medial axis capillary radius of the ROIs. The transform returns the skeleton of an image with the corresponding distance to a boundary in the foreground object. The transform was used on the binarized images of the ROIs using the `medial_axis` function in Python, housed in the `scikit-image` library [60]. Figure 2.12 shows the profiles generated for ROI 01 and ROI 02. It is shown that the medial axis is visually accurate, and the peritubular radius is mapped along its skeleton.

2.4.2 Red Blood Cell Linear Density

A similar approach in the segmentation of RBCs from the capillary space to measure their absorption values in all frames was done. The same steps described in section 2.2.3.1 was used, with the omission of k-means clustering of the pixels. This returned RBCs as they were seen in the capillary. The total RBC absorption value from each frame was used to calculate the estimated number of RBCs using Equation (2.5) with omittance of the y intercept. Visual comparison in estimating the number of red blood cells seen in the capillary space using the absorption value and Equation (2.5) can be seen in Figure 2.13. Estimation of the amount of red blood cells in different image sequences reflect and highlight the heterogeneity seen in linear density and oxygen concentration present in the capillary.

2.4.3 Red Blood Cell Velocity

The first 100 frames of ROI 01 was used to calculate the RBC velocity. Manual inspection resulted in the addition of 57, and the removal of 6, RBC coordinates, to give a total of 441

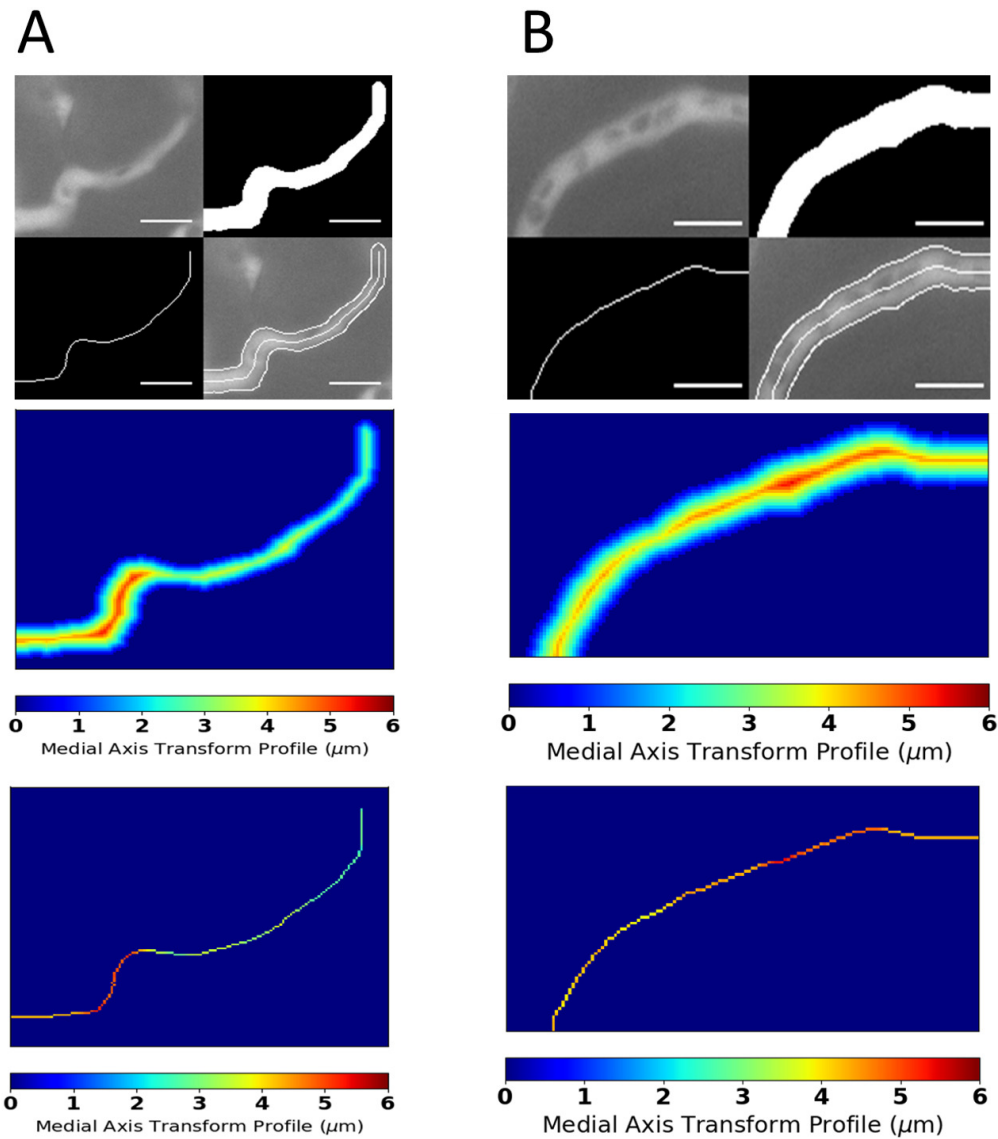


Figure 2.12: Medial axis transform of the ROIs. A) (Top) The original (top left), binarized image (top right), its skeleton (bottom left), and the skeleton and edges superimposed on the ROI 01 capillary (bottom right), its medial axis transform profile (middle), and the medial axis radius (bottom). B) The same images for the ROI 02 capillary. Scale bar = 20 μm .

recorded RBC centroids. The higher RBC linear density and increase in overlapping RBCs seen in the remaining frames in ROI 01 resulted in a higher uncertainty in locating centroids

of individual RBCs. Also, the uncertainty in knowing how many RBCs left and entered the capillary increased due to the limits of the capture speed of the images. Because of this, locating RBC centroids was subjected to only the first 100 frames of ROI 01. The omission of the centroid location of RBCs in ROI 02 was chosen as sequential frames containing identifiable individual RBCs were of limited quantity.

The average velocity of individual RBCs moving through the first 100 frames of the ROI 01 peritubular capillary can be seen in Figure 2.14. Average velocities were reported as the mean \pm the standard error of the mean (s.e.m.). The overall average of all the tracked RBC velocities was $230.81 \pm 9.88 \mu\text{m/s}$. Two distinct groupings of RBC velocity can be seen from Figure 2.14. The first group, tagged numbers one to 46, had an average velocity of $261.33 \pm 7.4 \mu\text{m/s}$, while the second, tagged numbers 47 to 58, had an average velocity of $113.80 \pm 4.8 \mu\text{m/s}$.

2.5 Discussion

Mapping of the medial axis radius over entire lengths of the peritubular capillaries can provide physiological insight into how AKI alters kidney function, with an emphasis on sepsis-induced AKI. The microcirculatory dysfunction seen in sepsis-induced AKI is highlighted by blood flow heterogeneity, which among other events, can be attributed to vasodilation of the capillaries or lack thereof. The ability to map the radius of the capillaries establishes capillary radius changes in a healthy renal system or a sepsis-induced AKI renal system and quantifies the difference in radius between capillaries that exhibit continuous flow and intermittent/no flow.

These physiological changes in capillary radius also have the potential to aid in understanding the effectiveness of therapeutic intervention for sepsis-induced AKI. Wu *et al.* [61] studied how inducible nitric oxide synthase inhibitor L-iminoethyl-lysine (L-NIL) affected capillary dysfunction and RNS generation in sepsis-induced AKI via cecal ligation and puncture. They reported that L-NIL significantly reversed the capillary perfusion alterations (defined as the increase in capillaries with continuous flow using IVVM), blocked RNS

generation, and reduced AKI. Similarly, Holthoff *et al.* [29] studied the effects of Resveratrol (RES) when administered to mice with sepsis-induced AKI. IVVM confirmed that RES prevented the change in the categorical distribution of cortical perfusion and the decline in RBC velocity. These studies could benefit from analyzing the change in the radii of the capillaries, as it could potentially lead to a better physio/pathophysiological understanding of the effects caused by AKI and the potential treatments to combat it.

In addition to aiding experimental results, estimation of the capillary radius is of importance when evaluating the delivery of oxygen from the RBCs to the tubular epithelial cells. Oxygen delivery for cellular metabolism is dependent on many factors, with one being the distance the oxygen molecules must travel to reach their desired destination. The development of mathematical models to describe this oxygen transport was first described by Krogh in 1919 [33], and subsequently further developed by Popel [52] and Secumb [36, 57]. Knowing the average radius can prove useful in simulating oxygen transport. These models incorporate physiological representations of the microvascular networks, *i.e.*, vessel radius, in their calculations to explain the flux of oxygen from the vessel centerline to the tissue boundary. The ability to estimate the capillary radius directly applies to these models. Change in this distance can alter the transit time of oxygen delivery, and thus may result in a change of cellular function and overall kidney performance. Changes in radius from healthy to diseased states of the microcirculation impacts mathematical models describing oxygen delivery to the renal system.

It was shown that the number of RBCs could be approximately estimated within the capillary space in both instances of low and high linear density. Accuracy in estimation in ROI 02 pertaining to low density images was confirmed via counting the number of RBCs observed. Counting RBCs was not possible for areas of high linear density due to the large amount of overlap and crowding. To address this issue, theoretical estimation of the number of possible RBCs within the capillary space was calculated. This was done by assuming the capillary can be represented as a uniform cylinder. The volume of the cylinder could be found by using the capillary length and the maximum medial radius value. With this information,

along with the known volume of a red blood cell and hematocrit level, the theoretical number of RBCs in the capillary could be compared with what was estimated using the images.

Physiologically-based assumptions play a role in RBC estimation as well. There exists a physiological limit to the number of RBCs that can be stacked on top of one another within the microcirculation. Geometric calculations could provide the bounds necessary when evaluating the number of RBCs seen in high density areas from a two dimensional perspective. A Beer's law experimental approach to light absorption may provide additional information, providing a non-invasively measured value to how many RBCs are present (according to light transmittance) when stacked. This upper limit combined with the RBC count obtained from absorption values could create a much more robust approach in estimating the number of RBCs seen in a capillary space.

The change in velocity may be attributed to the change in RBC linear density as frames progress in time. RBCs 1-46 moved through the capillary at a very low linear density, approximately 3.5 RBCs per frame (frame span 1-85), while RBCs 47-58 moved through the capillary at a linear density of approximately 9.6 RBCs per frame (frame span 86-100), almost a 3 fold increase in linear density from the earlier frames. The increase in linear density may cause a reduced velocity profile for the cells. As cells aggregate together, their overall movement could slow via interacting with one another or surrounding boundaries. It should be noted that the capillaries shown are under microcirculatory dysfunction from sepsis-induced AKI. Sepsis is known to cause a decrease in RBC deformability, a trait that may reduce the cells ability to easily pass through the capillary space [6]. In addition, sepsis is known to cause an increase in white blood cell adherence to the peritubular walls, and thus can contribute to a reduction in RBC velocity [6, 54]. These events may factor into the observed decrease in velocity.

There is limited reporting on RBC velocity in the renal microcirculation, and even fewer reports when not using the line scan method (see section 1.2). Holthoff *et al.* [29] reported that for healthy sham mice a RBC velocity in continuous flowing capillaries was $370 \pm 20 \mu\text{m/s}$, while sepsis-induced AKI mice via CLP saw a reduction in RBC velocity to $126 \pm 16 \mu\text{m/s}$. These velocities were calculated by inspecting 450 capillary segments and, if continuously flowing capillaries were identified, the velocity was calculated by measuring the

distance traveled by a single RBC over time. These results are similar to the result presented in this section, specifically the region of RBC velocity with a higher linear density.

Calculating RBC velocity in the healthy and diseased state can be of great aid in modeling the renal microcirculation. Accurate reporting of RBC velocity can provide approximate transit times oxygenated RBCs have to interact with the surrounding tissue. This can inform models of realistic physiological amounts of oxygen available for metabolic consumption, and in turn could describe hypoxic thresholds pertaining to the renal microcirculation.

The estimation of the number of RBCs combined with the known length of the capillary space under scrutiny can give the RBC linear density. Calculation of RBC linear density provides information regarding oxygen content seen within the capillaries. This content, or oxygen concentration, gives a descriptive feature to the renal microcirculation, as to the availability of O_2 for metabolic consumption. This information helps in the mathematical modeling of renal function. Similar as to how the radius of the capillaries aids in describing oxygen transit delivery lengths, the available oxygen concentration can be used to simulate scenarios that can describe hypoxic environments and how those environments affects renal function.

The ability to use image processing as a technique to capture kidney microhemodynamics was explored. Stabilization of the movement in the images gathered was alleviated by applying the Lucas-Kanade algorithm. Capillary radial mapping of the cortical peritubular capillaries was calculated using an L-infinity norm analysis to provide not only dimensions of the capillaries, but also the means of giving the broad location of red blood cells. Image segmentation was applied to capture red blood cells from the background. Once captured, velocity was calculated for individual flowing RBCs when applicable. Analysis of the intensity and absorption values of RBCs led to the formulation of a mathematical model that can be used as a measure of estimation of RBCs seen within the capillaries. This ability to estimate the number of RBCs can aide in the determination of how much oxygen is being delivered to the kidney for consumption.

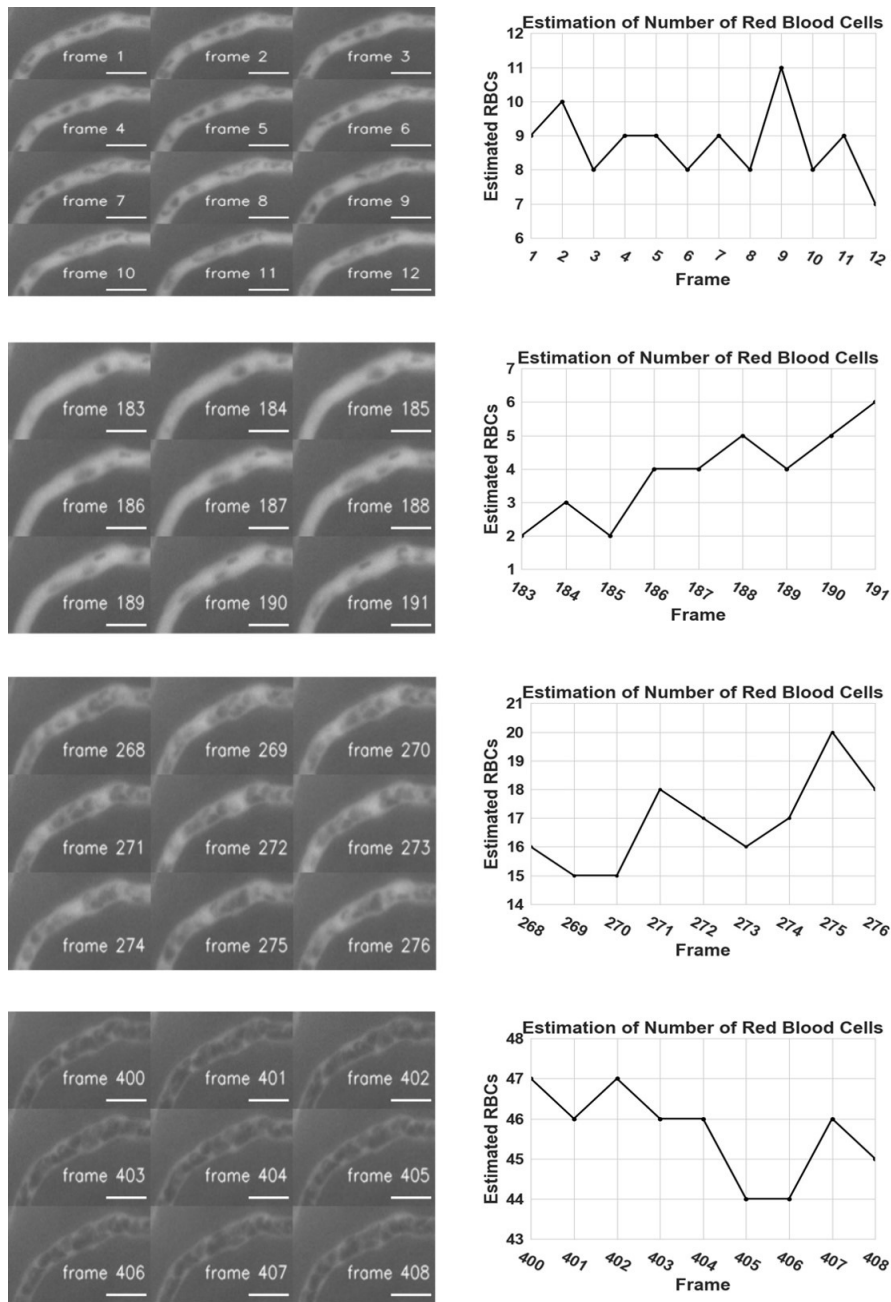


Figure 2.13: Visual comparison in estimating the number of red blood cells seen in the capillary space. Results of estimating the amount of red blood cells in different image sequences highlight the heterogeneity seen in linear density and oxygen concentration present in the capillary.

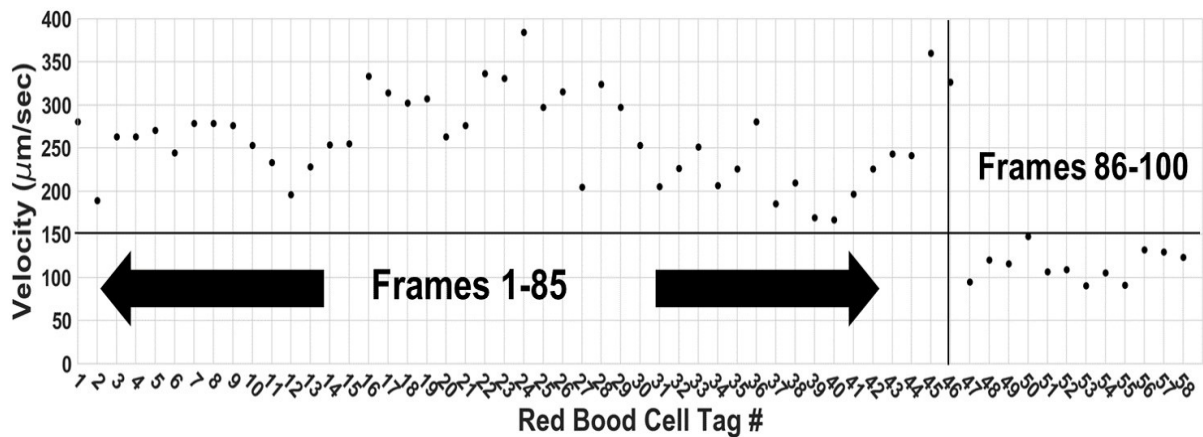


Figure 2.14: Individual RBC velocities seen traveling through the first 100 frames of ROI 01. Each RBC that passed through the capillary was given an ID tag number. Two average velocity groups are seen: RBC tag numbers 1 to 46 and RBCs tagged 47 to 58. RBC tag numbers 1 to 46 were seen in frames one through 85, and passed through the capillary with low linear density, as opposed to RBCs tagged 47 to 58. These were seen in frames 86 through 100, and passed through the capillary with a 3 fold higher linear density as that of the previously tagged RBCs.

3.0 Quantification of Mitochondrial Energetics in the Kidney

3.1 Introduction

The kidney is responsible for the removal of waste from the blood, the reabsorption of nutrients, regulating the balance of electrolytes and fluids, maintaining acid-base homeostasis, and regulating blood pressure. These tasks make the kidney one of the most energy demanding organs in the human body, causing it to have the highest resting metabolic rate and mitochondrial content, and the second-highest oxygen consumption, behind the heart [46].

These tasks, particularly the reabsorption of ions, nutrients, and glucose, rely on transporters and channels driven by ion gradients. Mitochondria provide the energy for Na^+/K^+ ATPase to generate these ion gradients across the cellular membrane. In the kidney, the proximal tubule, the loop of Henle, the distal tubule and the collecting duct all require and rely on active transport to reabsorb ions. The proximal tubules reabsorb 80% of the filtrate that passes through the glomerulus, and therefore have more active transport mechanisms and mitochondria than any other structure in the kidney. This makes proximal tubule function susceptible to hypoxic conditions, as it relies on aerobic respiration to produce ATP and meet its high energy demand.

Diseased states of the kidney, such as sepsis-induced AKI, disrupt mitochondrial function. Renal microcirculatory dysfunction has been reported in patients with sepsis-induced AKI. This dysfunction causes flow abnormalities, characterized by a decrease in continuous blood flow and an increase in vessels with intermittent or no flow [23]. This disrupts the delivery of oxygen to the mitochondria in the renal tubules. The reduction in ATP production decreases the available energy for the tubules to perform their tasks, and in turn, changes the bioenergetics of the system. The proximal tubules are a primary site of injury due to its high dependence on oxygen for metabolic consumption. The changes of microcirculatory flow and the consequences it and sepsis have on mitochondrial function must be addressed. This can be done by first understanding the physiological heterogeneity of the blood flow

and mitochondrial activity seen in healthy, normal kidney function. The monitoring of mitochondrial health is mostly experimental work [20]. New and promising techniques such as intravital video imaging can capture renal dynamics *in vivo* in real time, including microvascular flow and mitochondrial activity. Establishing reproducible metrics to quantify normal kidney state will provide the information needed to determine the extent of mitochondrial dysfunction and the change in heterogeneity of the diseased kidney.

3.1.1 Image Acquisition and Description

Intravital multi-photon microscopy (MPM) was used to capture the microvascular (capillary) space in the kidney and the mitochondrial activity in the tubules of a healthy C57BL/6J mouse. Images were captured following experimental procedure outlined by K. Dunn *et al.* [19] and were acquired through Dr. Hernando Gomez of UPMC, Department of Critical Care Medicine and Center of Critical Care Nephrology. Briefly, FITC-Dextran was intravenously administered to visualize the capillary space as shown in in Figure 3.1. Mitochondrial activity was assessed with the cationic lipophilic dye tetramethyl rhodamine methyl ester (TMRM). TMRM is a fluorescent dye used for measuring the mitochondrial membrane potential ($\Delta\Psi_m$), a parameter that relates to the capacity of a cell to generate ATP via oxidative phosphorylation. Therefore $\Delta\Psi_m$ can be used to measure cell health or injury.

TMRM accumulates in the mitochondrial membrane matrix space in an inverse proportion to $\Delta\Psi_m$, where a more negative $\Delta\Psi_m$ will accumulate more dye, and vice versa. Proton pumping from respiratory chain complexes I-V lead to a potential difference across the inner mitochondrial membrane. Protons are driven against their concentration gradient (out of the mitochondrial cytoplasm), only to flow back in upon ATP generation. This allows the uptake of TMRM to occur freely, and accumulate in the membrane matrix space [50]. The more uptake that occurs because of a more negative $\Delta\Psi_m$, results in a greater image intensity value. Imaging recorded 66 frames at 16 frames per second. Figure 3.1 shows the tubules and capillary space.

Inspection of the images taken revealed spatial heterogeneity in mitochondrial activity and blood volume. High and low intensity areas of TMRM emission were seen, similar to

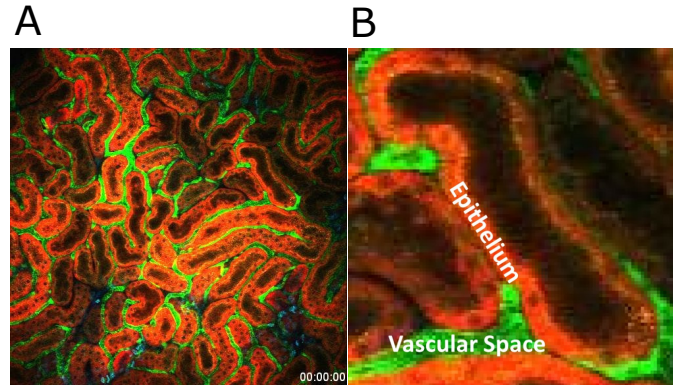


Figure 3.1: Visualization of mitochondrial function in the kidney. Multi-photon microscopy captures the A) renal microvascular space (green) and mitochondrial activity (red). The frame stamp is located in the bottom right hand corner. B) TMRM is visualised as a red color and is primarily taken up into the epithelium, which holds a high density of mitochondria. FITC-Dextran is visualized as green and resides within the vascular space.

that of higher density regions blood volume when compared to other areas. These spatial differences behave differently over time, seen in the images when viewed on a temporal scale.

3.2 Methods

3.2.1 Characterization of Blood Volume Space and Mitochondrial Activity

Description of the spatial heterogeneity seen in the images of the normal functioning kidney was determined by analyzing the average blood volume and mitochondrial activity pixel intensities. Each pixel contains a red channel intensity value and a green channel intensity value. If a pixel represents the capillary space, the green intensity value will be much larger in value compared to the red intensity value. The red intensity value of a pixel indicates the level of mitochondrial activity occurring, with low intensity indicting low activity, and high intensity indicating a high activity. Average blood volume pixel intensity

was calculated by evaluating the green channel of each pixel of each frame. Similarly, the mitochondrial activity pixel intensity was calculated using the red channel of each pixel of each frame. First, a circular mask with a radius half of the image length was applied to each image to remove the image frame identification stamp in the bottom right hand corner. A spectrum of different surface area sizes of the images were used to specify what pixels would be included when calculating the average channel intensities. These surface areas can be thought of as windows that allow us to see specific regions of the images. Average intensities were calculated using these surface areas to preserve the spatial relationship each pixel has with its surrounding neighbors. Intensity values correspond to the physiological aspects of the kidney. Mitochondrial activity is a factor of its surrounding environment, *i.e.*, the capillaries and blood volume seen in proximity to mitochondria. Analysis based solely on a pixel by pixel approach would disconnect the physiological relationship and misrepresent the system dynamics.

These windows spanned the entire length of the image, with their size being dictated by an arc length, θ (measured in degrees) oriented clockwise from the x axis. Different arc lengths used spanned from a θ of seven to 180 degrees. The minimum arc length of seven degrees was chosen because it represents the approximate diameter of the smallest renal tubule seen in the images. This ensures that the surface area visualization encompasses not just fragment intensities of the tubule but rather the entire tubule for analysis. Pixels enclosed in the surface areas were captured using MATLAB's *poly2mask* function from the image processing toolbox [37]. Figure 3.2 shows the progression from the initial frame to the desired surface area for analysis.

Spatial variations within the images was evaluated by rotating each surface area described by θ around their center point in one degree increments for 180 degrees. Average green and red channel pixel intensities were calculated for each rotation corresponding to each surface area size for each frame and were plotted against one another. Figure 3.3 shows the result of the average intensities collected using a surface area size θ of 60 degrees.

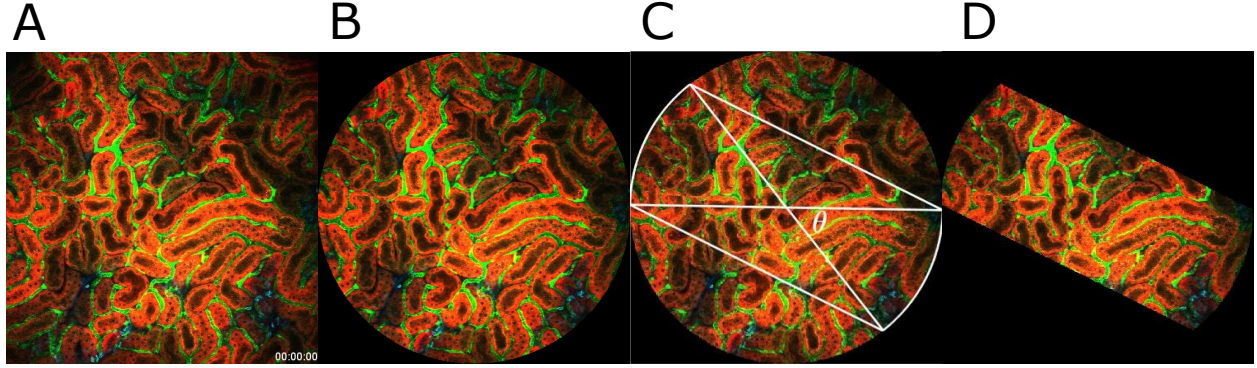


Figure 3.2: Images showing the image processing steps taken to create the desired surface area sizes used to calculate average pixel channel intensities. Images shown are A) The original image, B) application of a circular mask to remove the frame time stamp, C) the outline of the surface area window, defined in size by θ , and D) the final image used to calculate the average intensity.

3.2.2 Pixel Analysis using Geometric Ellipses

A minimum volume enclosing ellipse (MVEE) was computed for the mitochondrial activity vs blood volume intensity averages for each surface area size applied to the frames. An ellipse in center form can be represented by:

$$\varepsilon = \{x \in \mathbb{R}^2 | (x - c)^T E (x - c) \leq 1\} \quad (3.1)$$

Here x is a set of real points, c is the center of the ellipse ε , E is a positive semi-definite matrix, and T is the transpose. Methods described by Moshtagh [42] solve for the positive semi-definite matrix and the center point of the ellipse. Determination of the eigenvalues and eigenvectors of E gives the semi-major axes a , and semi-minor axes b as well as the rotation of the ellipse τ by solving:

$$a = 1/\sqrt{\lambda_1} \quad (3.2)$$

$$b = 1/\sqrt{\lambda_2} \quad (3.3)$$

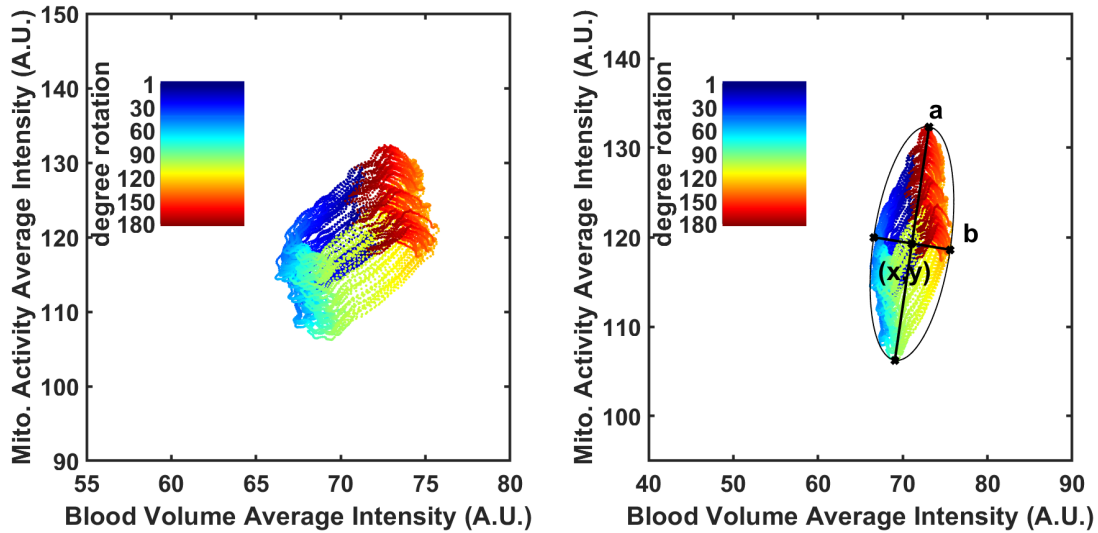


Figure 3.3: Average mitochondrial activity versus the blood volume pixel intensities. The surface area size that produced these average intensities had a θ of 60 degrees. The area was rotated 180 degrees in one degree increments. For each degree rotation, the average intensities were calculated for all frames. The color of each data point corresponds to the rotational degree that was used in calculations. A minimum volume enclosing ellipse was computed for the average pixel intensities. The parametric features of the ellipse are labeled with (x, y) being the ellipse center, a being the semi-major axis, and b being the semi-minor axis. The rotation of the ellipse (not labeled) is measured counter clockwise from the x axis.

$$\tau = \tan^{-1}(\epsilon_2, \epsilon_1) \quad (3.4)$$

Here λ_1 and λ_2 are the eigenvalues, with λ_1 being greater than λ_2 , ϵ_1 and ϵ_2 are the eigenvectors, and \tan^{-1} is the inverse tangent. The rotation of the ellipse was measured in degrees counterclockwise from the x axis. Because of this, the eigenvectors used in Equation (3.4) were chosen to represent a positive value for τ . The ellipse and its parametric features were plotted against the average green and red channel pixel intensities for each surface area window.

Figure 3.3 shows the MVEE, its semi-major and semi-minor axes, and its center point computed from the average intensities collected using a surface area size θ of 60 degrees.

3.3 Results

The parametric features for each ellipse found pertaining to the investigated window sizes are shown in Figure 3.4. Surface area size has been expressed as the fractional surface area coverage when compared to the original circle mask applied, described in Figure 3.2B. We see that the center x and y coordinates stay in relatively the same position after a change in location from a surface area of 1 to 0.7. An increase in both semi-major and semi-minor axis lengths is seen as surface area decreases, with the semi-major axis length increasing faster than the semi-minor axis. Oppositely, the rotation of the ellipse decreases as the surface area size decreases. The elliptical area calculated using the semi-major and minor axes was also found and plotted in Figure 3.4. The area increased as the surface area window size decreased.

The trends described above show the spatial heterogeneity seen in the blood volume and mitochondrial activity. As the surface area size used for characterization decreased, the semi-major axis rapidly increases, and the semi-minor axis increases, resulting in an increase in the overall area of the ellipses. This means a larger distribution in ratios of pixels that are identified as capillary space to pixels identified as renal tubules occurs. This shows that there exists spatial heterogeneity at and when different sections of the images are evaluated. If the images presented showed a homogeneous landscape, there would be little variation in the semi-major and semi-minor parametric features, and a uniform elliptic area would be seen, as opposed to the increase in elliptic area shown in Figure 3.4(right).

In addition to showing spatial heterogeneity, the parametric features can describe and show the spatial and temporal relationships of kidney function. Parametric features can spatially show where low and high mitochondrial activity is present in relation to blood volume. For example, in Figure 3.3(right), the semi major axes point stem from the center point to regions (described by the rotation of the surface area window) of low and high

mitochondrial activity. The same can be done for the blood volume intensity. Temporal changes in the functioning kidneys can also be measured as a result of the methods applied. Temporal changes are seen within the ellipse, where if there are large changes in the ratio of intensities as time progresses, the data recorded will be more distributed within the ellipse, and not as one concentric ellipse, i.e, data points would be recorded solely on the curve of the ellipse and not within the ellipse.

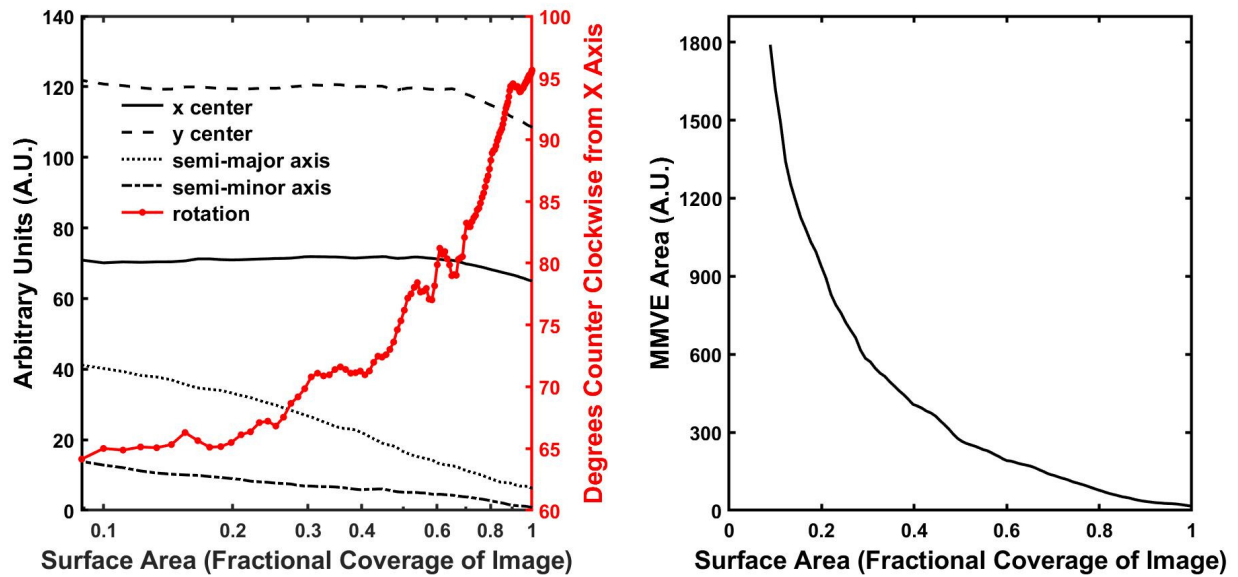


Figure 3.4: The parametric features of the ellipses enclosing the average mitochondrial and blood volume intensity values for all surface area sizes. The left hand plot shows the parametric features of the ellipse where the left side y axis (black) corresponds to the values for the x center coordinate, the y center coordinate, the semi-major axis, and the semi-minor axis and the right side y axis (red) corresponds to the values for the rotation of the ellipse. The x axis is shown in log scale to highlight the change in rotation as surface area size decreases. The right hand plot shows the minimum volume enclosing ellipse (MVEE) area for the mitochondrial activity and blood volume intensity values that were calculated as different surface area windows were rotated around the center point of the images. The area increases as the semi-major and semi-minor length increase, indicating different ratios of activity to volume intensities, and an increase in spatial distribution.

3.4 Discussion

Imaging *in vivo* of the kidney provides an excellent means to study renal dynamics, with multi-photon microscopy acting as the gold standard to collect these images. The use of fluorescent dyes FITC-Dextran and TMRM in tandem with MPM allow the blood volume space and the mitochondrial activity to be observed. TMRM allows the viewer to observe not only where mitochondrial activity is present but also how active mitochondria are, based on the concentration of TMRM in the mitochondrial membrane. The work of Hall [25, 26, 27] has extensively investigated the changes in mitochondrial function under normal renal function and ischemia-reperfusion injury (IRI) using multi-photon microscopy. IRI was mimicked by clamping the left renal artery, where cessation of blood flow caused a decrease in mitochondrial activity in the proximal tubules.

Visualization of the mitochondrial function and microcirculation of the renal system using MPM showed a landscape of spatial heterogeneity. This heterogeneity was evaluated by analyzing the average blood volume and mitochondrial activity pixel intensities pertaining to a wide range of spatial regions within the images. Once the average intensities were found, a minimum volume ellipse enclosed the data points when plotted against one another (Figure 3.3). Analysis of the parametric features allows for the spatial heterogeneity to be shown quantitatively in addition to qualitatively. It also quantitatively describes the spatial and temporal interactions between the blood volume and mitochondrial activity.

The images shown represent the normal functionality of mitochondria in the kidney. The methods created that analyze these images can also be applied to images showing sepsis-induced AKI. Mitochondrial injury has been clearly seen in sepsis via biochemical and structural studies [59]. This may be attributed to the hypoxia introduced from the dysfunctional microcirculation and the inflammatory effects brought on by sepsis. In addition to ATP production, mitochondria also maintain cellular functions including appropriate levels of reactive oxygen species. Superoxide is the main oxidant to be produced from respiratory complexes I, II, III of the mitochondria. Appropriate levels of ROS are kept by manganese superoxide dismutase.

Elevated levels of nitric oxide are associated with sepsis, and react with superoxide to form peroxynitrite, a reactive nitrogen species [16]. This causes harm to the host cell and can lead to death.

Results of mitochondrial dysfunction associated with sepsis-induced AKI would be highlighted using MPM and suitable fluorophores. The uptake of TMRM would decrease in the mitochondrial membrane matrix in areas that exhibit hypoxia and/or higher levels of ROS and RNS generation. Quantifying both healthy and injured kidney energetics and blood flow could shed light on the physiological relationships seen between the two states.

4.0 Summary and Future Work

4.1 Summary

Intravital video microscopy has allowed the renal microcirculation and the mitochondrial activity to be analyzed. Acute kidney injury, namely sepsis-induced AKI, causes microcirculatory and mitochondrial dysfunction to occur [22], where the the blood flow becomes sluggish or even stopped/no flow in regional areas. The lack of oxygen, (as well as the detrimental effects brought on by sepsis, such as the increase in ROS and RNS species) causes the mitochondria to dysfunction, yielding an overall decrease in renal function.

The heterogeneity seen in the dysfunctional microcirculation was studied using IVVM. The use of image processing created methods to map the capillary radius of the capillaries, calculate the velocity of RBCs in continuous flow, and estimate the linear density of RBCs. The results collected can be used to better inform researchers in how the microcirculation behaves as well as how oxygen delivery and availability changes from healthy to diseased states.

Mitochondrial activity and blood volume dynamics were evaluated using MPM and image processing. The spatial and temporal heterogeneity was quantified in an effort to explain potential variability in kidney function and to characterize the normal kidney state. Different sized regions within the images were analyzed to evaluate this heterogeneity. The methods created to explain the heterogeneity can be applied to healthy and diseased states of renal function, with the motive to compare and contrast the difference seen between the two. The approach may give insight as to how energy consumption changes when AKI has caused changes to the microcirculation.

4.2 Future Work

The directions the future works of these projects can take is wide. The foremost important step is an increase in data collection. Collecting more images of the kidney in both the healthy and diseased states is necessary to improve the current work presented. More images can bolster the information obtained from the current work and can aid in explaining the differences seen when the kidney succumbs to renal disease.

A specific area in need of attention is addressing how overlapping RBCs influence estimation. Preliminary work has identified that representation of RBC intensity values as absorption values (see Section 2.2.3.3) may give better insight in how to label RBCs that are overlapped. In an absorption value approach, the overlapped RBCs will have a higher absorption value than single RBCs, although the value may not follow a linear approach. From the experimental viewpoint, the RBCs will have a light saturation limit, contributing to the assumption that overlapped RBCs will follow a nonlinear absorption value.

The nonlinear relationship with overlapped RBCs and absorption value indicates that a nonlinear term must be added to the model formed from assessing single RBC absorption values. The linear model does not take into account the saturation limit the RBCs and the images themselves have. Michaelis-Menten kinetics was explored as a means to address both the linear non overlapping RBC absorption values and the nonlinear overlapping absorption values. Attempts to incorporate this kinetic model was tried, although more analysis is needed to prove meaningful results. Moving forward, a robust model that incorporates both linear and nonlinear terms must be used to explain RBC absorption values along with a more in depth understanding of the light saturation limits the RBCs have. These tools would greatly enhance the ability in estimation of RBCs in the capillaries and how this number affects kidney function.

The analysis of the capillary radius, oxygen concentration, and mitochondrial activity all contribute to the understanding of how the renal system works, under normal and diseased states. This information can directly be used in the building of mathematical models that explore and simulate oxygen delivery and consumption in the kidney.

This would aid in understanding the heterogeneity seen in the microcirculatory dynamics, the changes seen when there is a challenge in oxygen, and how the renal system responds to hypoxic conditions.

Bibliography

- [1] D. Allen, T. Caswell, N. Keim, and C. van der Wal. trackpy: Trackpy v0.3.2. 2016. doi: 10.5281/zenodo.60550. URL <https://doi.org/10.5281/zenodo.60550>.
- [2] R. Alobaidi, R. K. Basu, S. L. Goldstein, and S. M. Bagshaw. Sepsis-Associated Acute Kidney Injury. *Seminars in Nephrology*, 35(1):2–11, 2015. ISSN 15584488. doi: 10.1016/j.semnephrol.2015.01.002.
- [3] N. Arulkumaran, C. S. Deutschman, M. R. Pinsky, B. Zuckerbraun, P. T. Schumacker, H. Gomez, A. Gomez, P. Murray, and J. A. Kellum. Mitochondrial function in sepsis. *Shock*, 45(3):271–281, 2016. ISSN 15400514. doi: 10.1097/SHK.0000000000000463.
- [4] S. L. Ashworth, R. M. Sandoval, G. A. Tanner, and B. A. Molitoris. Two-photon microscopy: Visualization of kidney dynamics. *Kidney International*, 72(4): 416–421, 2007. ISSN 00852538. doi: 10.1038/sj.ki.5002315. URL <http://www.kidney-international.org>.
- [5] S. Baker and I. Matthews. Lucas-Kanade 20 Years On: A Unifying Framework. *International Journal of Computer Vision*, 56(3):221–255, 2004. ISSN 09205691. doi: 10.1023/B:VISI.0000011205.11775.fd. URL <http://www.ri.cmu.edu/projects/project>.
- [6] R. Bateman, M. Sharpe, M. Singer, C. Ellis, R. M. Bateman, M. D. Sharpe, M. Singer, and C. G. Ellis. The Effect of Sepsis on the Erythrocyte. *International Journal of Molecular Sciences*, 18(9):1932, sep 2017. ISSN 1422-0067. doi: 10.3390/ijms18091932. URL <http://www.mdpi.com/1422-0067/18/9/1932>.
- [7] R. Bellomo, J. A. Kellum, and C. Ronco. Acute kidney injury. *The Lancet*, 380 (9843):756–766, 2012. ISSN 1474547X. doi: 10.1016/S0140-6736(11)61454-2. URL [http://dx.doi.org/10.1016/S0140-6736\(11\)61454-2](http://dx.doi.org/10.1016/S0140-6736(11)61454-2).
- [8] R. Bellomo, J. A. Kellum, C. Ronco, R. Wald, J. Martensson, M. Maiden, S. M. Bagshaw, N. J. Glassford, Y. Lankadeva, S. T. Vaara, and A. Schneider. Acute kidney injury in sepsis. *Intensive Care Medicine*, 43(6):816–828, 2017. ISSN 14321238. doi: 10.1007/s00134-017-4755-7.
- [9] R. Berndt, T. J., Thompson, J. R., Kumar. The Regulation of Calcium, Magnesium, and Phosphate Excretion by the Kidney. In *Brenner and Rector’s The Kidney (Tenth Edit)*. Elsevier Inc., 2012.
- [10] P. Bhargava and R. G. Schnellmann. Mitochondrial energetics in the kidney. *Nature Reviews Nephrology*, 13(10):629–646, 2017. ISSN 1759507X. doi: 10.1038/nrneph.2017.107. URL <http://www.genome.jp/kegg/>.

- [11] J. V. Bonventre and L. Yang. Cellular pathophysiology of ischemic acute kidney injury. *Journal of Clinical Investigation*, 121(11):4210–4221, 2011. ISSN 00219738. doi: 10.1172/JCI45161. URL <http://www.jci.org>.
- [12] G. Bradski. The opencv Library. *Dr Dobb's J. Software*, 25:120–125, 2000.
- [13] A. R. Chade. Renal vascular structure and rarefaction. *Comprehensive Physiology*, 3(2):817–831, 2013. ISSN 20404603. doi: 10.1002/cphy.c120012.
- [14] A. R. Chade. Small Vessels, Big Role. *Hypertension*, 69(4):551–563, 2017. ISSN 0194-911X. doi: 10.1161/hypertensionaha.116.08319.
- [15] J. C. Crocker and D. G. Grier. Methods of Digital Video Microscopy for Colloidal Studies. *JOURNAL OF COLLOID AND INTERFACE SCIENCE*, 179:298–310, 1996.
- [16] S. Cuzzocrea, E. Mazzon, R. Di Paola, E. Esposito, H. Macarthur, G. M. Matuschak, and D. Salvemini. A Role for Nitric Oxide-Mediated Peroxynitrite Formation in a Model of Endotoxin-Induced Shock. *Journal of Pharmacology and Experimental Therapeutics*, 319(1):73 LP – 81, oct 2006. doi: 10.1124/jpet.106.108100. URL <http://jpet.aspetjournals.org/content/319/1/73.abstract>.
- [17] D. De Backer, D. O. Cortes, K. Donadello, and J. L. Vincent. Pathophysiology of microcirculatory dysfunction and the pathogenesis of septic shock. *Virulence*, 5(1):73–79, 2014. ISSN 21505608. doi: 10.4161/viru.26482.
- [18] K. Doi. Role of kidney injury in sepsis. *Journal of Intensive Care*, 4(1):1–6, 2016. ISSN 20520492. doi: 10.1186/s40560-016-0146-3. URL <http://dx.doi.org/10.1186/s40560-016-0146-3>.
- [19] K. W. Dunn, T. A. Sutton, and R. M. Sandoval. Live-Animal Imaging of Renal Function by Multiphoton Microscopy. *Current protocols in cytometry*, 83:12.9.1–12.9.18, 2012. ISSN 19349300. doi: 10.1002/cpcy.32. URL <http://www.currentprotocols.com/>.
- [20] N. J. Ekbal, A. Dyson, C. Black, and M. Singer. Monitoring Tissue Perfusion, Oxygenation, and Metabolism in Critically Ill Patients. *CHEST*, 143(6):1799–1808, jun 2013. ISSN 0012-3692. doi: 10.1378/chest.12-1849. URL <https://doi.org/10.1378/chest.12-1849>.
- [21] R. A. Fenton and J. Praetorius. 2 - Anatomy of the Kidney. In *Brenner and Rector's The Kidney, 2-Volume Set*, pages 42–82.e8. Elsevier Inc., tenth edit edition, 2018. doi: 10.1016/B978-1-4557-4836-5.00002-3.
- [22] H. Gómez and J. A. Kellum. Sepsis-induced acute kidney injury. *Current Opinion in Critical Care*, 22(6):546–553, 2016. ISSN 1070-5295. doi: 10.1097/MCC.0000000000000356.

- [23] H. Gomez, C. Ince, J. Hotchkiss, P. Pickkers, D. De Backer, J. A. Kellum, and D. Payen. A Unified Theory of Sepsis-Induced Acute Kidney Injury. *Shock*, 41(1):3–11, 2013. ISSN 1073-2322. doi: 10.1097/shk.000000000000052.
- [24] P. Guerci, B. Ergin, and C. Ince. The macro- and microcirculation of the kidney. *Best Practice and Research: Clinical Anaesthesiology*, 31(3):315–329, 2017. ISSN 1532169X. doi: 10.1016/j.bpa.2017.10.002. URL <https://doi.org/10.1016/j.bpa.2017.10.002>.
- [25] A. M. Hall and B. A. Molitoris. Dynamic Multiphoton Microscopy: Focusing Light on Acute Kidney Injury. *Physiology*, 29(5):334–342, 2014. ISSN 1548-9213. doi: 10.1152/physiol.00010.2014.
- [26] A. M. Hall, C. Crawford, R. J. Unwin, M. R. Duchon, and C. M. Peppiatt-Wildman. Multiphoton Imaging of the Functioning Kidney. *Journal of the American Society of Nephrology*, 22(7):1297–1304, 2011. ISSN 1046-6673. doi: 10.1681/ASN.2010101054.
- [27] A. M. Hall, G. J. Rhodes, R. M. Sandoval, P. R. Corridon, and B. A. Molitoris. In vivo multiphoton imaging of mitochondrial structure and function during acute kidney injury. *Kidney International*, 83(1):72–83, 2013. ISSN 15231755. doi: 10.1038/ki.2012.328.
- [28] B. Halliwell and M. Whiteman. Measuring reactive species and oxidative damage in vivo and in cell culture: How should you do it and what do the results mean? *British Journal of Pharmacology*, 142(2):231–255, 2004. ISSN 00071188. doi: 10.1038/sj.bjp.0705776. URL www.nature.com/bjp.
- [29] J. H. Holthoff, Z. Wang, K. A. Seely, N. Gokden, and P. R. Mayeux. Resveratrol improves renal microcirculation, protects the tubular epithelium, and prolongs survival in a mouse model of sepsis-induced acute kidney injury. *Kidney International*, 81(4):370–378, 2012. ISSN 00852538. doi: 10.1038/ki.2011.347.
- [30] J. J. Kang, I. Toma, A. Sipos, F. McCulloch, and J. Peti-Peterdi. Quantitative imaging of basic functions in renal (patho)physiology. *American Journal of Physiology-Renal Physiology*, 291(2):F495–F502, 2006. ISSN 1931-857X. doi: 10.1152/ajprenal.00521.2005. URL <http://www.ajprenal.org>.
- [31] L. Kang. The image stabilizer plugin for {ImageJ}. 2008.
- [32] D. Kleinfeld, P. P. Mitra, F. Helmchen, and W. Denk. Fluctuations and stimulus-induced changes in blood flow observed in individual capillaries in layers 2 through 4 of rat neocortex. *Proceedings of the National Academy of Sciences*, 95(26):15741–15746, 1998. ISSN 0027-8424. doi: 10.1073/pnas.95.26.15741.
- [33] A. Krogh. The number and distribution of capillaries in muscles with calculations of the oxygen pressure head necessary for supplying the tissue. *The Journal of physiology*, 52(6):409–15, 1919. ISSN 0022-3751.

- [34] F.-C. Kuo, M.-S. Wu, C.-T. Huang, F.-C. Hu, H.-H. Liou, H.-Y. Chen, H.-C. Pan, W.-S. Yang, C.-Y. Lin, J.-P. Tsai, Z.-h. You, T.-S. Lai, C.-C. Kao, V.-C. Wu, Y.-F. Yang, C.-C. Shiao, J.-J. Wang, K.-C. Lu, K.-H. Lee, C.-C. Huang, W.-C. Kan, T.-C. Chen, J.-H. Lin, C.-F. Chang, P.-C. Wu, C.-J. Weng, K.-D. Wu, K.-L. Chien, T.-M. Huang, H. Y.-H. Lin, C.-M. Chen, C.-H. Wu, C.-J. Wu, C.-Y. Sun, and W.-D. Hsu. Nationwide epidemiology and prognosis of dialysis-requiring acute kidney injury (NEP-AKI-D) study: Design and methods. *Nephrology*, 21(9):758–764, sep 2015. ISSN 13205358. doi: 10.1111/nep.12670. URL <http://doi.wiley.com/10.1111/nep.12670>.
- [35] M. Le Dorze, M. Legrand, D. Payen, and C. Ince. The role of the microcirculation in acute kidney injury. *Current Opinion in Critical Care*, 15(6):503–508, 2009. ISSN 10705295. doi: 10.1097/MCC.0b013e328332f6cf.
- [36] A. Lo, A. J. Fuglevand, and T. W. Secomb. Oxygen delivery to skeletal muscle fibers: effects of microvascular unit structure and control mechanisms. *American Journal of Physiology - Heart and Circulatory Physiology*, 285(3):H955–H963, 2003. ISSN 0363-6135. doi: 10.1152/ajpheart.00278.2003.
- [37] MATLAB Image Processing Toolbox. Matlab image processing toolbox. 2018b.
- [38] M. Matsumoto, T. Tanaka, T. Yamamoto, E. Noiri, T. Miyata, R. Inagi, T. Fujita, and M. Nangaku. Hypoperfusion of peritubular capillaries induces chronic hypoxia before progression of tubulointerstitial injury in a progressive model of rat glomerulonephritis. *Journal of the American Society of Nephrology*, 15(6):1574–1581, 2004. ISSN 10466673. doi: 10.1097/01.ASN.0000128047.13396.48.
- [39] J. A. McCormick and D. H. Ellison. The Distal Convolute Tubule. *Comprehensive Physiology*, 5(1):45–98, jan 2015. ISSN 20404603. doi: 10.1002/cphy.c140002.
- [40] M. Miranda, M. Balarini, D. Caixeta, and E. Bouskela. Microcirculatory dysfunction in sepsis: pathophysiology, clinical monitoring, and potential therapies. *American Journal of Physiology - Heart and Circulatory Physiology*, 311(1):H24–H35, 2016. ISSN 0363-6135. doi: 10.1152/ajpheart.00034.2016. URL <http://ajpheart.physiology.org/lookup/doi/10.1152/ajpheart.00034.2016>.
- [41] B. A. Molitoris and R. M. Sandoval. Intravital multiphoton microscopy of dynamic renal processes. *American Journal of Physiology-Renal Physiology*, 288(6):F1084–F1089, jun 2005. ISSN 1931-857X. doi: 10.1152/ajprenal.00473.2004. URL <http://www.physiology.org/doi/10.1152/ajprenal.00473.2004>.
- [42] N. Moshtagh. Minimum volume enclosing ellipsoids. *Convex Optimization*, 111 (January):1–9, 2005. ISSN 0022-3239. doi: 10.1.1.116.7691.
- [43] D. B. Mount. The Transport of Sodium, Chloride, and Potassium. In *Brenner and Rector’s The Kidney (Tenth Edit)*. Elsevier Inc., 2012.

- [44] K. A. Munger, C. K. Kost, B. M. Brenner, and D. A. Maddox. The Renal Circulations and Glomerular Ultrafiltration. In *Brenner and Rector's The Kidney*, pages 94–137. Elsevier Inc., tenth edit edition, 2012. ISBN 9781416061939. doi: 10.1016/B978-1-4160-6193-9.10003-X.
- [45] N. Nourbakhsh and P. Singh. Role of renal oxygenation and mitochondrial function in the pathophysiology of acute kidney injury. *Nephron - Clinical Practice*, 127(1-4): 149–152, 2014. ISSN 16602110. doi: 10.1159/000363545.
- [46] D. J. Pagliarini, S. E. Calvo, B. Chang, S. A. Sheth, S. B. Vafai, S. E. Ong, G. A. Walford, C. Sugiana, A. Boneh, W. K. Chen, D. E. Hill, M. Vidal, J. G. Evans, D. R. Thorburn, S. A. Carr, and V. K. Mootha. A Mitochondrial Protein Compendium Elucidates Complex I Disease Biology. *Cell*, 134(1):112–123, 2008. ISSN 00928674. doi: 10.1016/j.cell.2008.06.016.
- [47] T. L. Pallone, Z. Zhang, and K. Rhinehart. Physiology of the renal medullary microcirculation. *American Journal of Physiology - Renal Physiology*, 284(2):F253–F266, 2003. ISSN 0363-6127. doi: 10.1152/ajprenal.00304.2002.
- [48] S. M. Parikh, Y. Yang, L. He, C. Tang, M. Zhan, and Z. Dong. Mitochondrial Function and Disturbances in the Septic Kidney. *Seminars in Nephrology*, 35(1):108–119, 2015. ISSN 15584488. doi: 10.1016/j.semnephrol.2015.01.011. URL <http://dx.doi.org/10.1016/j.semnephrol.2015.01.011>.
- [49] F. Pedregosa, G. Varoquaux, A. Gramfort, V. Michel, B. Thirion, O. Grisel, M. Blondel, P. Prettenhofer, R. Weiss, V. Dubourg, J. Vanderplas, A. Passos, D. Cournapeau, M. Brucher, M. Perrot, and É. Duchesnay. Scikit-learn: Machine Learning in Python. *J. Mach. Learn. Res.*, 12:2825–2830, nov 2011. ISSN 1532-4435. URL <http://dl.acm.org/citation.cfm?id=1953048.2078195>.
- [50] S. W. Perry, J. P. Norman, J. Barbieri, E. B. Brown, and H. A. Gelbard. Mitochondrial membrane potential probes and the proton gradient: a practical usage guide. *BioTechniques*, 50(2):98–115, feb 2011. ISSN 0736-6205. doi: 10.2144/000113610. URL <http://www.ncbi.nlm.nih.gov/pmc/articles/PMC3115691/>.
- [51] J. Peti-Peterdi, K. Kidokoro, and A. Riquier-Brison. Intravital imaging in the kidney. *Current Opinion in Nephrology and Hypertension*, 25(3):168–173, 2016. ISSN 14736543. doi: 10.1097/MNH.0000000000000219.
- [52] A. S. Popel. HEORY OF OXYGEN TRANSPORT TO TISSUE. *Crit Re v Biomed Eng*, 293(6):H3740–H3749, 1989. ISSN 0363-6135. doi: 10.1152/ajpheart.00009.2007.
- [53] E. H. Post, J. A. Kellum, R. Bellomo, and J. L. Vincent. Renal perfusion in sepsis: from macro- to microcirculation. *Kidney International*, 91(1):45–60, 2017. ISSN 15231755. doi: 10.1016/j.kint.2016.07.032. URL <http://dx.doi.org/10.1016/j.kint.2016.07.032>.

- [54] R. M. Sandoval and B. A. Molitoris. Intravital multiphoton microscopy as a tool for studying renal physiology and pathophysiology. *Methods*, 128:20–32, 2017. ISSN 10959130. doi: 10.1016/j.ymeth.2017.07.014.
- [55] S. Sawhney and S. D. Fraser. Epidemiology of AKI: Utilizing Large Databases to Determine the Burden of AKI. *Advances in Chronic Kidney Disease*, 24(4):194–204, 2017. ISSN 15485609. doi: 10.1053/j.ackd.2017.05.001.
- [56] J. Schindelin and Arganda-Carreras. Fiji: an open-source platform for biological-image analysis. *Nature methods*, 9(7):676, 2012.
- [57] T. W. Secomb, R. Hsu, E. Y. H. Park, and M. W. Dewhurst. Green’s Function Methods for Analysis of Oxygen Delivery to Tissue by Microvascular Networks. Technical Report 11, 2004.
- [58] D. M. Small, W. Y. Sanchez, M. J. Hickey, and G. C. Gobe. Multiphoton fluorescence microscopy of the live kidney in health and disease. *Journal of biomedical optics*, 19(2):020901, 2014. ISSN 1560-2281. doi: 10.1117/1.
- [59] O. Takasu, J. P. Gaut, E. Watanabe, K. To, R. E. Fagley, B. Sato, S. Jarman, I. R. Efimov, D. L. Janks, A. Srivastava, S. B. Bhayani, A. Drewry, P. E. Swanson, and R. S. Hotchkiss. Mechanisms of cardiac and renal dysfunction in patients dying of sepsis. *American Journal of Respiratory and Critical Care Medicine*, 187(5):509–517, 2013. ISSN 1073449X. doi: 10.1164/rccm.201211-1983OC. URL www.atsjournals.org.
- [60] S. van der Walt, J. L. Schönberger, J. Nunez-Iglesias, F. Boulogne, J. D. Warner, N. Yager, E. Gouillart, T. Yu, and T. scikit-image contributors. scikit-image: image processing in {P}ython. *PeerJ*, 2:e453, 2014. ISSN 2167-8359. doi: 10.7717/peerj.453.
- [61] L. Wu, N. Gokden, and P. R. Mayeux. Evidence for the Role of Reactive Nitrogen Species in Polymicrobial Sepsis-Induced Renal Peritubular Capillary Dysfunction and Tubular Injury. *Journal of the American Society of Nephrology*, 18(6):1807–1815, 2007. ISSN 1046-6673. doi: 10.1681/asn.2006121402.
- [62] T. Yamamoto, T. Tada, S. V. Brodsky, H. Tanaka, E. Noiri, F. Kajiya, and M. S. Goligorsky. Intravital videomicroscopy of peritubular capillaries in renal ischemia. *American Journal of Physiology-Renal Physiology*, 282(6):F1150–F1155, 2002. ISSN 1931-857X. doi: 10.1152/ajprenal.00310.2001. URL <http://www.ajprenal.org>.
- [63] A. Zarbock, H. Gomez, and J. A. Kellum. Sepsis-induced acute kidney injury revisited: Pathophysiology, prevention and future therapies. *Current Opinion in Critical Care*, 20(6):588–595, 2014. ISSN 15317072. doi: 10.1097/MCC.000000000000153.
- [64] L.-A. Zhang. *MODEL-BASED DECISION SUPPORT FOR SEPSIS ENDOTYPES*. PhD thesis, University of Pittsburgh, 2017.